Techniques for Molecular Detection: From Mid-Infrared Spectrometers to Nanopore Devices

Thesis by
Changsoon Choi

In Partial Fulfillment of the Requirements for the
Degree of
Doctor Of Philosophy in Electrical Engineering

Caltech

CALIFORNIA INSTITUTE OF TECHNOLOGY
Pasadena, California

2025
Defended May 20, 2025

© 2025

Changsoon Choi
ORCID: 0009-0005-4037-8643

ACKNOWLEDGEMENTS

ABSTRACT

This thesis presents the development and characterization of three distinct molecular detection platforms aimed at improving accessibility and scalability. These systems utilize optical and electrical sensing techniques to analyze solid, liquid, and gas-phase samples, addressing challenges in portability, cost-effectiveness, and throughput.

First, a compact mid-infrared spectrometer was developed using a continuously variable filter composed of Ge/BaF$_2$ distributed Bragg reflectors and a 2-D microbolometer array. This design enables high signal-to-noise ratio measurements across the long-wave infrared region (7.5–10.5 μm) without requiring moving parts. The system was calibrated using polymer samples and validated through spectral measurements of gases and liquids using gas cells and attenuated total reflection configurations. The results demonstrate good agreement with commercial Fourier transform infrared (FTIR) spectrometers while maintaining a significantly smaller form factor and lower cost.

Next, a tunable diode laser absorption spectroscopy system was implemented for methane detection. The system uses wavelength-modulated distributed feedback lasers and lock-in detection to achieve high sensitivity. Both free-space and fiber-optic configurations were developed, with detection limits down to 0.5 ppm-m for the free-space system. Real-time gas monitoring was demonstrated using retroreflectors and beam-steering optics, enabling multi-point detection with a single source-detector pair.

Finally, a design for a multiplexed nanopore detector was proposed to improve throughput. Electric properties of solid-state nanopores were investigated through analytical modeling, numerical simulations, and experimental conductance measurements. A new sensing architecture incorporating embedded electrodes was introduced. Simulations confirmed that this design enables independent detection of translocation events at each pore. Prototype devices were fabricated to validate the concept.

Together, these platforms offer scalable and accessible alternatives to conventional molecular detection systems, with potential applications in environmental monitoring, industrial gas sensing, and real-time molecular diagnostics.

PUBLISHED CONTENT AND CONTRIBUTIONS

1. Jeon, T., Nateghi, A., Choi, C., Jewell, J. & Scherer, A. Compact mid-infrared spectrometer using continuously variable infrared filter and microbolometer array for simple and fast measurement of molecular mid-IR spectra. *Advanced Optical Materials* **12,** 2302241 (2024).
    C.C. developed custom software for spectrometer control and data processing, conducted FDTD simulations, assembled the hardware, and contributed to data collection and manuscript preparation.

TABLE OF CONTENTS

LIST OF ILLUSTRATIONS

Chapter 1

INTRODUCTION

Chemical detectors play a pivotal role in modern society, enabling rapid and reliable identification of chemical species across a wide range of applications. These systems translate the presence of a target molecule into a measurable signal and have profoundly impacted areas including healthcare, environmental monitoring, and industrial safety. Historically, chemical sensing systems were complex and confined to laboratories. However, the field has seen progress in making detection technologies more compact, affordable, and user-friendly.

Some of the most successful chemical detectors have become ubiquitous in daily life. The glucometer, for instance, revolutionized diabetes management by allowing patients to monitor blood glucose levels at home using enzymatic reactions and electrochemical detection [1, 2]. In homes and workplaces, carbon monoxide (CO) detectors provide critical safety monitoring by alerting occupants to odorless, potentially lethal gas leaks. These devices exemplify the potential for chemical sensing tools to move from specialized laboratories into the hands of ordinary users.

In recent years, advances in materials science, microfabrication, and photonics have opened new doors for developing accessible, high-performance detectors [3–6]. Wearable sensors can now continuously monitor biomarkers through sweat or interstitial fluids [7]. Low-cost air quality monitors equipped with optical or electrochemical sensors have become increasingly common in urban settings, enabling real-time pollution tracking [8]. Miniaturized spectroscopic systems and lab-on-a-chip platforms are beginning to offer laboratory-grade capabilities in portable formats [9]. These developments reflect a broader trend. Chemical sensing technologies are becoming more compact, cost-effective, and accessible.

1.1 Objective of this Thesis

In this thesis, three distinct chemical detection methods are developed. They are all attempts in seeking better trade-offs between cost, size, sensitivity, and selectivity in order to provide more accessible chemical detectors.

First, a compact mid-infrared (mid-IR) spectrometer capable of identifying a wide range of organic materials is described in Chapter 2. Fourier transform infrared

(FTIR) spectrometers can identify small amount of molecule from a fingerprint region spectrum, but high costs and large sizes limit their availability in our daily life. The compact mid-IR spectrometer is to provide similar measurements with a fraction of the cost and footprint.

Next, Chapter 3 describes a tunable-diode-laser absorption spectroscopy (TDLAS) system optimized for highly sensitive, rapid methane sensing via wavelength modulation and lock-in detection. As methane emission's contribution to the global warming increases, monitoring the emission is becoming more crucial. Unlike conventional infrared spectroscopy-based detectors that only monitor the near vicinity, the system suggested in this thesis is capable of monitoring multiple locations with a single source-detector pair. With this approach, larger number of detectors can be deployed with the same cost, leading to lower green house gas emissions.

Finally, possibilities of versatile solid-state nanopore detectors are explored. Nanopore detectors, especially biological nanopore detectors, are widely used in sequencing DNAs [10, 11]. However, these detectors can be functionalized to detect proteins or pathogens and have the potential to be applied in a variety of applications [12, 13]. However, their density (number of detectors in a package) is somewhat limited because only one pore can be implemented on a membrane. In this thesis, a novel detection method and device design towards multiplexed detector is discussed. First, Chapter 4 describes an attempt to understand the properties of the nanopores through DC conductivity measurements. Then Chapter 5 presents ongoing efforts to realize a proof-of-concept multiplexed array capable of simultaneous, multi-site analysis with a single source–detector pair.

Reference

1. Teymourian, H., Barfidokht, A. & Wang, J. Electrochemical glucose sensors in diabetes management: An updated review (2010–2020). *Chemical Society Reviews* **49,** 7671–7709 (2020).

2. Ghosh, M. & Bora, V. R. Evolution in blood glucose monitoring: A comprehensive review of invasive to non-invasive devices and sensors. *Discover Medicine* **2,** 74 (2025).

3. Hierlemann, A., Brand, O., Hagleitner, C. & Baltes, H. Microfabrication techniques for chemical/biosensors. *Proceedings of the IEEE* **91,** 839–863 (2003).

4. Zhang, C., Qu, M., Fu, X. & Lin, J. Review on microscale sensors with 3D engineered structures: Fabrication and applications. *Small Methods* **6,** 2101384 (2022).

5. Fenzl, C., Hirsch, T. & Wolfbeis, O. S. Photonic crystals for chemical sensing and biosensing. *Angewandte Chemie International Edition* **53,** 3318–3335 (2014).

6. Butt, M. A., Mateos, X. & Piramidowicz, R. Photonics sensors: A perspective on current advancements, emerging challenges, and potential solutions. *Physics Letters A* **516,** 129633 (2024).

7. Yang, Y. & Gao, W. Wearable and flexible electronics for continuous molecular monitoring. *Chemical Society Reviews* **48,** 1465–1491 (2019).

8. Marć, M., Tobiszewski, M., Zabiegała, B., Guardia, M. D. L. & Namieśnik, J. Current air quality analytics and monitoring: A review. *Analytica Chimica Acta* **853,** 116–126 (2015).

9. Yang, Z., Albrow-Owen, T., Cai, W. & Hasan, T. Miniaturization of optical spectrometers. *Science* **371,** eabe0722 (2021).

10. Branton, D. *et al.* The potential and challenges of nanopore sequencing. *Nature Biotechnology* **26,** 1146–1153 (2008).

11. Kono, N. & Arakawa, K. Nanopore sequencing: Review of potential applications in functional genomics. *Development, Growth & Differentiation* **61,** 316–326 (2019).

12. Nilsson, J., Lee, J. R. I., Ratto, T. V. & Létant, S. E. Localized Functionalization of Single Nanopores. *Advanced Materials* **18,** 427–431 (2006).

13. Lepoitevin, M., Ma, T., Bechelany, M., Janot, J.-M. & Balme, S. Functionalization of single solid state nanopores to mimic biological ion channels: A review. *Advances in Colloid and Interface Science* **250,** 195–213 (2017).

Chapter 2

COMPACT MID-INFRARED SPECTROMETER USING CONTINUOUSLY VARIABLE INFRARED FILTER AND MICROBOLOMETER ARRAY

This section has been adopted from a published paper [1].

2.1 Introduction

Spectroscopy in the mid-infrared (mid-IR) region is useful for determining functional groups of molecules [2]. Because functional groups of molecules have characteristic absorption bands in the mid-IR region, these bands are useful for analyzing the molecular structure. Therefore, mid-IR spectroscopy can be used in the pharmaceutical industry [3, 4], gas analysis [5, 6], and pollution detection [7, 8]. However, the conventional mid-IR spectrometer (Fourier-transform infrared spectroscopy, FTIR) requires a complex optical system, which limits measurement of the sample in situ. Portable infrared spectrometers in the near-infrared region (800 nm to 2.5 µm wavelength of light) have been developed well due to advancements in technology related to near-infrared detectors [9] and light sources [10, 11]. Material deposition techniques for optical films has also progressed, with several materials available for deposition in the near-infrared region [12, 13]. Additionally, there is a requirement for portable spectrometers in the long-wave infrared (LWIR) region, which ranges from 7.5 to 14 µm. This range is called the fingerprint region because distinctive absorption bands of molecules in this region allow for accurate identification of their molecular structures [14]. Compact spectrometer for the LWIR region have not been well-developed due to challenges in material selection, high cost of light sources, and bulky cooled detectors. Recently, uncooled microbolometers have been developed as detectors, demonstrating good sensitivity in the LWIR region [15, 16]. However, there has been limited research conducted toward the development of portable spectrometers in the LWIR region.

Studies on the development of mid-infrared sensors in the LWIR region us- ing surface plasmons [17–19] or dielectric metasurfaces [20, 21] have been conducted. Because these approaches use an enhanced near-field, it can increase the light and molecules interaction, thus increasing the sensitivity of the system. However, using the near-field enhancement for molecular detection requires a sample coating on

the substrate, which limits the measurement of multiple samples with one system. Additionally, this approach is costly due to the requirement for precise nanofabrication of the resonator for each measurement. There has been research focused on mid-IR chemical identifiers that are based on plasmonic structures and combined with machine learning algorithms [22]. However, this method utilizes broad resonance peaks from the filters, which makes it challenging to obtain an accurate chemical spectrum. Therefore, in terms of accurately capturing the transmittance spectra of molecules, this approach has limitations. The mid-infrared optical filter with gradual change of cavity thickness can be a good solution for the light dispersion elements of miniaturized mid-IR spectrometers [23]. In our previous work, silicon/air mirrors, utilizing free-standing silicon films, were used to create continuously variable optical filters in the mid-IR range. However, this approach encountered a challenge: the bowing of the silicon film. Such deformation limited our ability to accurately correct data across the entire 2D array of detectors, resulting in noisy spectra acquired from single rows of the detector.

In this chapter, we introduce germanium (Ge) and barium fluoride (BaF_2) as materials for filter deposition, which results in a continuously variable filtered wavelength across the 2D detector array. This enables the accurate measurement of spectra, integrated from data across 13,000 pixels (130 rows and 100 columns), capable of capturing the subtle features of the absorption spectra of molecules. The large refractive index contrast between Ge and BaF_2 enables the free spectral range to cover the entire LWIR region. The filter exhibits a sharp optical transmittance peak, with the peak position gradually shifting along the filter in the direction where the cavity length varies. A thermal emitter, producing incoherent broadband mid-IR light from blackbody radiation, is used as the light source. As light passes through the filter, it encounters varying cavity lengths, resulting in the transmission of different wavelengths from distinct regions of the filter. These wavelengths are then directed to the corresponding pixels on the microbolometer array. By integrating the information from all the pixels of microbolometer array and applying a deconvolution process, high signal-to-noise ratio mid-IR spectra of various samples can be obtained. The wavelength range of our spectrometer is from 7.5 to 10.5 µm. By adopting attenuated total reflection (ATR) for liquids and utilizing a gas cell for gases, our method also enables the measurement of absorption spectra for liquid and gas samples. Finally, we compare the mid-IR spectra obtained from our new spectrometer with spectra measured from FTIR to illustrate that our compact spectrometer can accurately capture all the features present in molecular absorption spectra.

2.2   Results and Discussion

By combining continuously variable mid-IR optical filters with a 2D microbolometer array, it is possible to create a compact mid-IR spectrometer capable of real-time analysis. A continuously variable filter is used to filter out different wavelengths of light, which are subsequently collected by the 2D detector array. Integration of the data gathered from the 13,000 pixels of the array enable the generation of spectra with a high signal-to-noise (SNR) ratio. The filter is manufactured by making a distributed Bragg reflector (Bragg mirror) using Ge and BaF_2, which is transparent in the LWIR region. The space between the two Bragg mirrors is gradually changed to allow the transmission of continuously varying wavelengths of LWIR light (Figure 2.1(a)). The filtered wavelengths of LWIR light are subsequently collected by a 2D microbolometer array. This setup allows for the visualization of the sample molecules' absorption lines on the detector array when sample is placed, as illustrated in Figure 2.1(b). In our experiment, the filter size is 1 cm along the gap-variation direction and the width of the filter is 1 cm. Furthermore, we used a Ge lens with a diameter of 1.27 cm and an f/1 focal ratio for collimation, and another Ge lens with similar specifications for imaging purposes. The distance between the imaging lens and the microbolometer is $\approx$ 1.27 cm. Additionally, the distance between the filter and the imaging lens is $\approx$ 10 cm. The calibration sample is polypropylene (PP) with a thickness of $\approx$ 40 μm. The absorption spectrum of PP using 1 cm^{-1} resolution FTIR is shown in white graph in Figure 2.1(b). The characteristic peaks of PP can be observed as dark lines on the image. The absorption lines appear curved due to stress on the filter during manufacturing, while the absorption itself is caused by the polypropylene (PP) sample. The calibration sample allows for wavelength mapping of each pixel within the detector array. Subsequently, the absorption spectrum of the sample can be obtained by integrating and averaging the data from all pixels at each wavelength. Furthermore, employing the deconvolution algorithm aids in sharpening the obtained spectrum. Figure 2.1(c) shows the transmittance spectrum of PP measured by our compact mid-IR spectrometer system after averaging all the pixels at each wavelength and deconvolution signal process.

A continuously variable mid-IR filter is designed to target LWIR band (7.5 to 14 μm). This LWIR band is the fingerprint region of molecules, and it is the region where the absorption peaks of moisture in the air can be avoided. The center wavelength of filter is designed to be 9 μm, and the thickness of Ge and BaF2 layers is $\lambda/(4n)$, where λ is center wavelength and n is refractive index of each layer (Figure 2.2(a)). The Ge layer is deposited using a radio-frequency (RF) sputter system and BaF_2 is
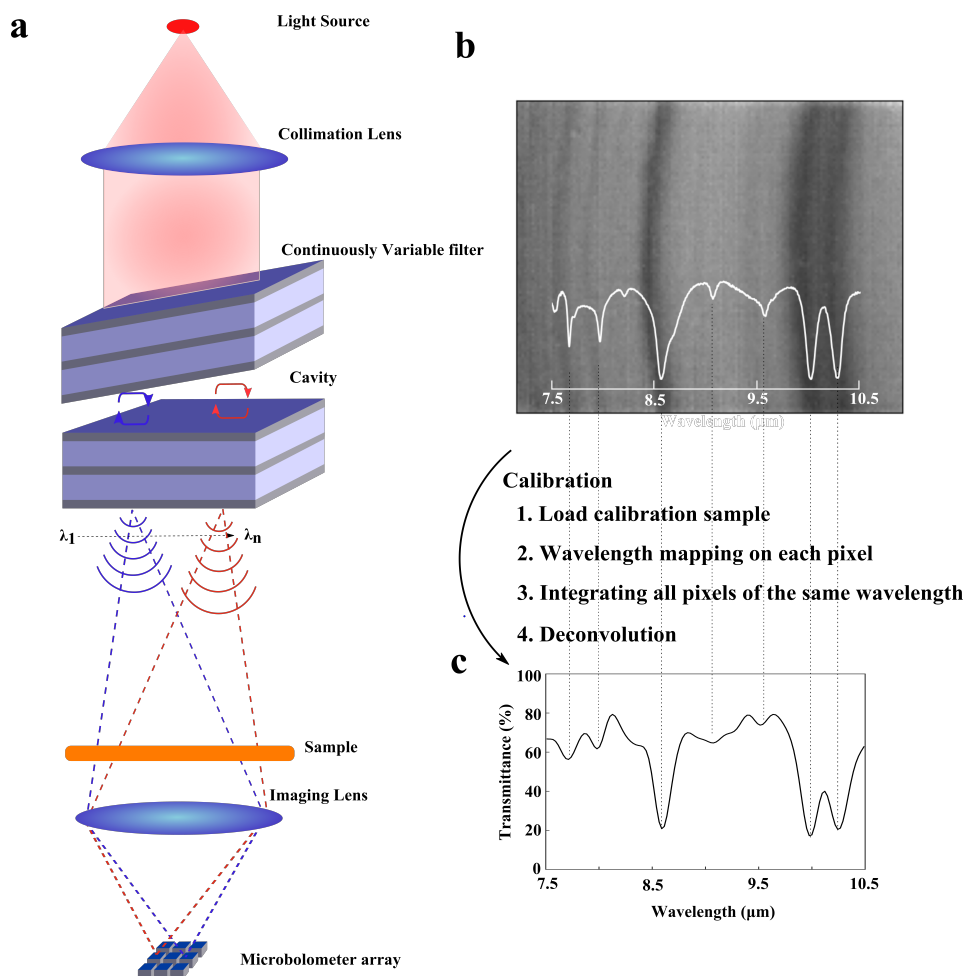
Figure 2.1: Compact mid-IR spectrometer and spectral measurements. (a) The optical system of a compact mid-IR spectrometer is constructed using a continuously variable mid-IR filter and a 2D microbolometer array. (b) An image captured from the microbolometer array shows clear dark lines corresponding to three main peaks (8.6, 10.02, and 10.28 μm) and other lighter lines when a polypropylene sample is placed on the optical path. The white spectrum represents the transmittance spectrum of polypropylene measured from a FTIR (1 cm^{-1} resolution). (c) The transmittance spectrum of polypropylene obtained from our compact spectrometer is generated by averaging all the pixels at each wavelength and deconvolution process.

deposited using a thermal evaporator. A gradual change in the air-cavity gap between two DBRs is achieved using a two-step photolithography process. Specifically, two different thicknesses of spacers are patterned on both edges of a single DBR, and it combines with another DBR to form the filter, resulting in a gradual change in the air cavity between the two DBRs. One spacer is shown in Figure 2.2(b) and cross-sectional view of one DBR is shown in Figure 2.2(c). The transmission spectra as a function of cavity gap thicknesses are shown in Figure 2.2(d). As cavity gap increase from 3 to 7 µm, resonance peak position changes from 7 to 12.4 µm. When the cavity gap exceeds 7.2 µm, second harmonic peaks begin to appear in the long-wave infrared (LWIR) range.

Figure 2.2(e) shows the calculated resonance peak positions relative to the cavity gap, along with the corresponding Full Width at Half Maximum (FWHM) values of each peak. The reflectivity of the Distributed Bragg Reflector (DBR) mirror is highest at the center wavelength of 9 µm, resulting in the smallest FWHM value in this region. As we move toward the edges of the free- spectral range, the FWHM values increase. In this experiment, we limited the spectrometer's range from 7.5 to 10.5 µm because the FWHM values increase dramatically when the wavelength exceeds 11 µm. This FWHM value play a crucial role in determining the resolution of spectrometer system and can be reduced by increasing the reflectivity of DBRs. However, this can also lead to a decrease in the intensity of transmitted light, resulting in a lower signal-to-noise ratio spectrum. In this experiment, two pairs of Ge/BaF$_2$ are used to make a balance between high transmittance and sufficient resolution for detecting several molecules. Further reduction in FWHM values can be achieved in the future by using a high-efficiency light source or a more sensitive detector. Additionally, to expand the spectral range of spectrometer, one solution would be preparing two different filter: one for the from 7.5 to 10.5 µm range and another for the from 10.5 to 14 µm range, and then combine them. Figure 2.2(f) shows measured transmittance spectra at various cavity lengths of the filter using FTIR. The widths of these spectra are broader than calculated values because the FTIR beam size covers a range of cavity gaps during the measurement.

To achieve a high signal-to-noise ratio transmittance spectrum, multiple data points from a 2D microbolometer pixel array were averaged. To assign corresponding wavelengths to each pixel, a calibration sample of polypropylene is used. Figure 2.3(a) illustrates the absorption lines of polypropylene when placed on the optical paths, captured by a microbolometer array consisting of 13,000 pixels (130 rows
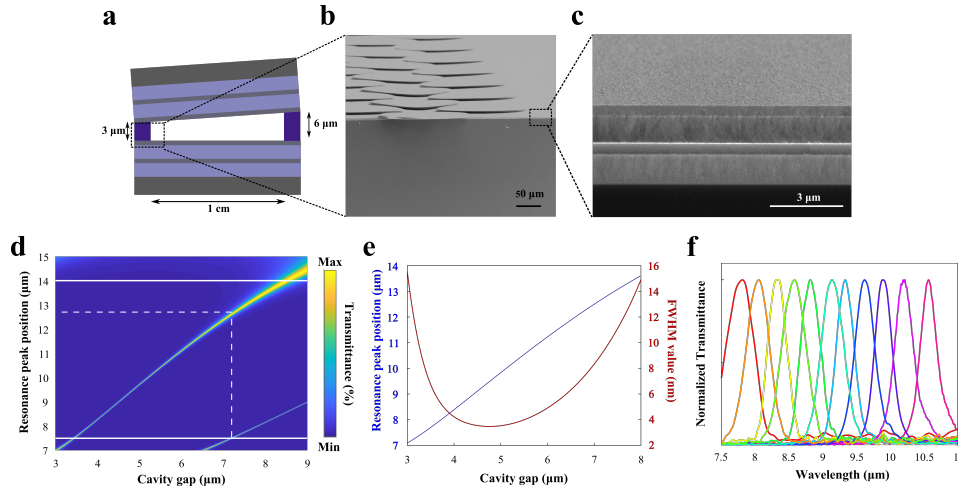
Figure 2.2: Design and characterization of a continuously variable air-cavity filter. (a) The schematic diagram illustrates a continuously variable air-cavity filter. The angle is exaggeratedly portrayed. (b) The SEM image shows a spacer on one side of the filter. (c) The SEM image shows a cross-sectional view of Ge-BaF2 Bragg's mirror. (d) The transmittance (%) map at the mid-IR region as the air cavity gap between two DBRs change. The second harmonic peak comes into the LWIR region as the cavity gap increases to 7.2 μm. The dashed line indicates the transmittance peak position at 12.7 μm when the cavity gap is 7.2 μm. (e) The blue line in the graph shows the changes in resonance peak position as the cavity gap varies and the red line shows FWHM values of peaks as the cavity gap varies. (f) The measured transmittance peaks at different regions of the filter using an FTIR spectrometer. The width of the peak is wide due to the FTIR beam size covering some range of cavity gaps.

and 100 columns). The three darkest lines correspond to absorption peaks of polypropylene at wavelengths of 8.6, 10.02, and 10.28 μm, while two weaker lines are observed at 7.66 and 7.96 μm. The curvature of the absorption lines is a result of the stress on the filter during the wafer bonding process of two separate distributed Bragg reflector (DBR) mirrors. The mapping of corresponding wavelength (μm) at every pixel position (x, y) is achieved by using a quadratic function based on the known pixel-to-wavelength relation obtained from the absorption lines in Figure 2.3(a) (using five absorption lines). By fitting the quadratic function to the data points representing the pixel positions and their corresponding wavelength, the parameters of the quadratic function can be determined. This mapping allows for the accurate assignment of wavelengths to each pixel position within the microbolometer array. Figure 2.3(b) presents a plot showing the resulting solutions when substituting each grid of "x" and "y" values into the quadratic function. The color represents the
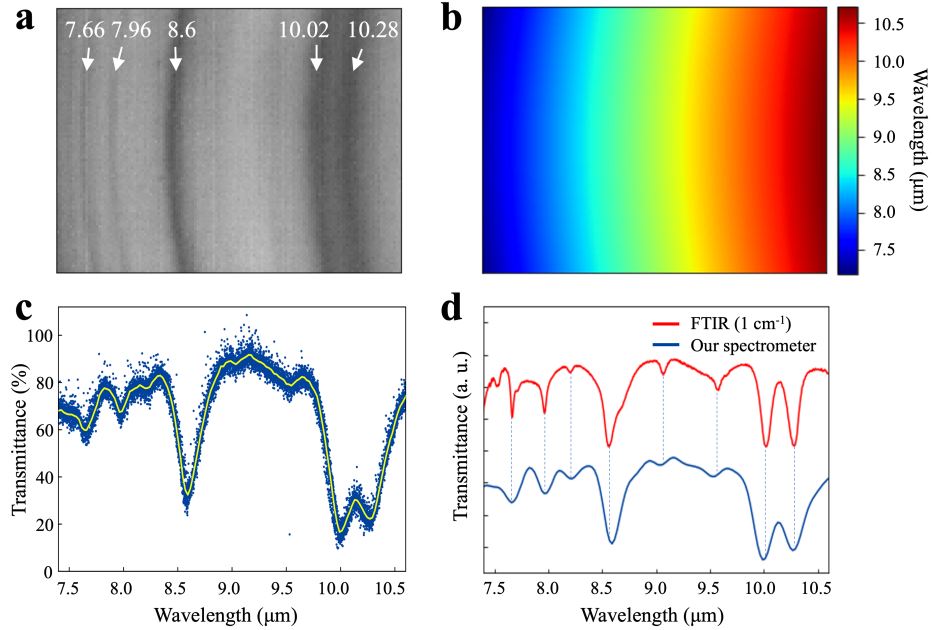
Figure 2.3: Wavelength calibration and spectral reconstruction. (a) The spectrometer captured absorption lines of polypropylene, and the numbers on top indicate the wavelengths (μm) of these absorption lines. The image consists of 13,000 pixels arranged in 130 rows and 100 columns. (b) A wavelength mapping of all the pixels based on the calibration lines in (a). (c) A plot showing the wavelength versus intensity of all 13,000 pixels (represented as blue dots) and spectrum obtained by averaging the values at each wavelength (depicted as a yellow curve) (d) A comparison between the polypropylene transmittance spectrum measured using 1 cm^{-1} resolution FTIR (red plot) and the spectrum obtained from our spectrometer after averaging the values at each wavelength and undergoing a deconvolution process.

corresponding wavelength (μm), demonstrating that the wavelength lines follow the same curvature as depicted in Figure 2.3(a). All 13,000 intensity values versus wavelengths are plotted by the blue dots in Figure 2.3(c). By averaging the values at each wavelength, a single spectrum of polypropylene is obtained, as shown by the yellow graph in Figure 2.3(c). Given that the uncooled microbolometer array is susceptible to thermal noise, this type of integration process is useful in minimizing noise and increasing the signal-to-noise level.

Following the calibration of the system using polypropylene, the transmittance spectrum of other samples can be measured. In Figure 2.4(a), the measurement of a different polymer film (polystyrene) is depicted.

In addition to measuring polymer film samples, gas and liquid molecules can also

be measured using the spectrometer. To measure the transmittance spectrum of gas molecules, a gas cell is placed on the optical path, as shown in Figure 2.4(b). Germanium (Ge) windows, transparent to mid-IR light and located at the ends of the gas cell, are coated with an anti-reflection layer to optimize light transmission with minimal losses. The transmittance spectrum of methane gas molecules (100% concentration) in the gas cell is shown in Figure 2.4(c), clearly showing the absorption feature of methane in the 7.5 to 8.5 μm range.

Absorption spectra of liquids can also be measured using an ATR approach. For liquid measurements in transmission mode, a liquid cell can be used. However, an excess of liquid in transmittance measurements can saturate the absorption peaks, making them indistinct and difficult to identify, while too little liquid can evaporate quickly, making it difficult to measure accurately. This issue can be solved by using ATR.

The blackbody radiation from the light source can be guided inside a Ge crystal (Figure 2.4(d)). The light can then internally reflect inside the crystal, generating an evanescent wave in the air. This is demonstrated in the Finite-Difference Time-Domain (FDTD) simulation data shown in Figure 2.4(e). When a liquid is dropped onto the surface of the Ge crystal, absorption of both the evanescent wave and the bound light within the crystal by the liquid occurs simultaneously, matching the boundary condition. Consequently, this altered light then travels to the continuously variable filter. The penetration depth of the evanescent wave, which is the distance at which the amplitude of the light decays to $1/e$ of its initial value, depends on the incident angle, as shown in Figure 2.4(f). This makes it suitable for measuring surface sensitive measurement such as biological materials [24–26]. Figure 2.4(g) shows the absorption spectrum of liquid acetone when analyzed using ATR on the surface of the Ge crystal.

2.3 Conclusion

These initial results are promising, indicating that our simple and fast spectrometer can measure mid-IR spectra of various types of molecules (polymer film, gas, and liquid). The continuous variable filter, which features a gradual change of cavity length between two Ge/BaF$_2$ mirrors, allows us to detect transmittance spectra of molecules at LWIR using a microbolometer array. High signal-to-noise ratio spectra can be obtained by integrating all the data from pixel array and deconvolution process. This system does not require any moving parts and minimizes the number
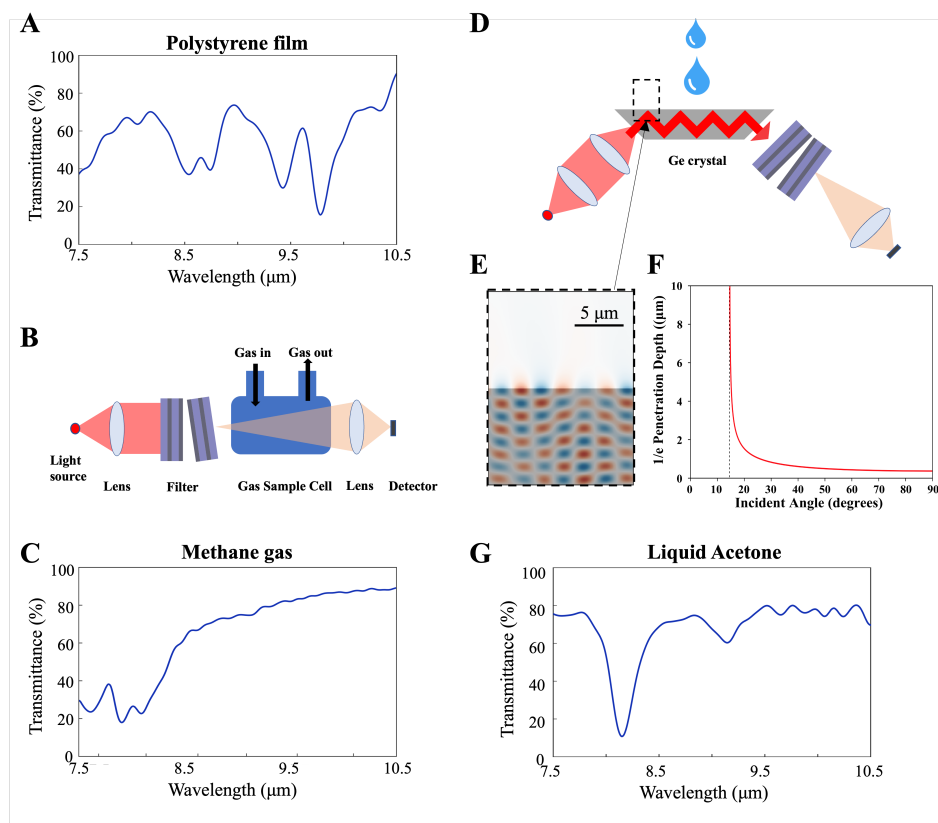
Figure 2.4: Solid, gas, and liquid phase sample measurements. (a) Transmittance measurement of polystyrene film. The sample is located in the same position as the PP measurement shown in Figure 2.1(a). (b) The schematic shows the optical setup for gas measurement, with the gas sample cell located between the filter and imaging lens. The gas fills the inside of the cell. (c) Transmittance spectrum of methane gas filled inside the cell. (d) The schematic shows the optical setup for liquid measurement. A Ge crystal with both edges angled at 45°was used for attenuated total reflection (ATR). Blackbody radiation enters the Ge crystal and bounces within it, coming out from the other edge and passing through a continuous variable filter. (e) The FDTD simulation image showing the electric field travels inside the Ge crystal at a 45°angle to the surface, creating an evanescent wave on the air part. (f) The graph shows the length from the air/Ge surface to the point where the intensity of light decays to $1/e$ of the incoming light. The $1/e$ penetration depth for a 45°incident angle with a wavelength of 9 μm is 541 nm. (g) Transmittance spectrum of acetone when liquid acetone is dropped on the surface of the Ge crystal.

of optical elements, resulting in an improved simplicity compared to conventional mid-IR spectrometers, while maintaining robust and reliable performance. Spectral acquisition relies on the speed of the microbolometer array, operating at 9 Hz in our case, which is faster than FTIR that requires mirror scanning. We have demonstrated a reasonable spectral resolution with our compact mid-IR spectrometer, and further improvement can be achieved by optimizing optical. Additionally, for accurate quantitative analysis, it is essential to calibrate each pixel precisely, accounting for gain and offset, and to ensure the light sources are uniform. To avoid spectral distortion from non-uniform solid samples, adjusting the sample position relative to the light source might be beneficial. Once fully optimized, our mid-IR spectrometer will enable real-time detection of molecules with a simple and cost-effective system.

2.4 Experimental Section

Ge/BaF2 Filter Fabrication: Ge membranes were deposited with RF sputtering system, which provides a refractive index of ≈ 4.2 in the mid-IR region. The BaF_2 was deposited by using thermal evaporation and the refractive index was ≈ 1.4 in the mid-IR region. The target wavelength for mirror deposition was 9 μm, resulting in a physical thickness of 562 nm for the Ge layer and 1.6 μm for the BaF_2 layer. To create 3 and 6 μm spacers on one DBR, photolithography with SU-8 negative photoresist was employed. After applying spacers on one DBR, the two DBRs were bonded by pressing them against each other and baked at 130 °C. The baking process softens the SU-8 polymer slightly, allowing it to adhere to the other side of the DBR.

FTIR Measurement: In FTIR measurements, a Jasco FTIR spectrometer was used with a resolution of 1 cm^{-1}. The detector employed was triglycine sulfate (TGS). To measure the optical properties of the continuously variable filter, a slit with a width of ≈ 1 mm was placed in front of the filter. The filter was then moved from the 3 μm air-cavity side to the 6 μm cavity side to measure the optical properties at different locations on the filter.

FDTD Simulation: Simulation of the electric field distribution at the Ge-Air interface (Figure 2.4(e)) was performed with the finite-difference time-domain (FDTD) method [27] using an open-source software package MEEP [28]. In the simulation space, the $y = 0$ plane separated the Ge and Air layer. Refractive indices of Ge and Air layers were set to 4.0 and 1.0, respectively. The light source was a plane wave with a wavelength of 9 μm. The polarization was set to be transverse-electric (TE). The wave was incident to the interface at a 45° angle from the Ge side. The electric

field distribution was saved to visualize the intensity ($|E|^2$).

Measurement of Absorption Spectra of Molecules: The Seek Compact XR camera was used for the microbolometer array. The spectral range of this camera was from 7.5 to 14 μm and the frame rate was ≈ 9 Hz, which enables nine frames acquisition in 1 s.

Reference

1. Jeon, T., Nateghi, A., Choi, C., Jewell, J. & Scherer, A. Compact mid-Infrared spectrometer using continuously variable infrared filter and microbolometer array for simple and fast measurement of molecular mid-IR spectra. *Advanced Optical Materials* **12,** 2302241 (2024).

2. Pavia, D. L., Lampman, G. M., Kriz, G. S. & Vyvyan, J. R. Introduction to spectroscopy (2015).

3. Bunaciu, A. A., Aboul-Enein, H. Y. & Fleschin, S. Application of Fourier transform infrared spectrophotometry in pharmaceutical drugs analysis. *Applied Spectroscopy Reviews* **45,** 206–219 (2010).

4. Lin, S.-Y. & Wang, S.-L. Advances in simultaneous DSC–FTIR microspectroscopy for rapid solid-state chemical stability studies: some dipeptide drugs as examples. *Advanced Drug Delivery Reviews* **64,** 461–478 (2012).

5. Bak, J. & Clausen, S. FTIR emission spectroscopymethods and procedures for real time quantitative gas analysisin industrial environments. *Measurement Science and Technology* **13,** 150 (2001).

6. Materazzi, S. & Vecchio, S. Evolved gas analysis by infrared spectroscopy. *Applied Spectroscopy Reviews* **45,** 241–273 (2010).

7. Pejcic, B., Myers, M. & Ross, A. Mid-infrared sensing of organic pollutants in aqueous environments. *Sensors* **9,** 6232–6253 (2009).

8. Gowen, A., Tsenkova, R., Bruen, M. & O'donnell, C. Vibrational spectroscopy for analysis of water for human use and in aquatic ecosystems. *Critical Reviews in Environmental Science and Technology* **42,** 2546–2573 (2012).

9. Vardi, A. *et al.* Near infrared quantum cascade detector in GaN/AlGaN/AlN heterostructures. *Applied Physics Letters* **92** (2008).

10. Siesler, H. W., Ozaki, Y., Kawata, S. & Heise, H. M. *Near-infrared spectroscopy: Principles, instruments, applications* (John Wiley & Sons, 2008).

11. Zhu, C., Fu, X., Zhang, J., Qin, K. & Wu, C. Review of portable near infrared spectrometers: Current status and new techniques. *Journal of Near Infrared Spectroscopy* **30,** 51–66 (2022).

12. Fainstein, A., Lanzillotti-Kimura, N. D., Jusserand, B. & Perrin, B. Strong optical-mechanical coupling in a vertical GaAs/AlAs microcavity for subterahertz phonons and near-infrared light. *Physical Review Letters* **110,** 037403 (2013).

13. Patrini, M. *et al.* Optical response of one-dimensional (Si/SiO2)m photonic crystals. *Journal of Applied Physics* **92,** 1816–1820 (2002).

14. Larkin, P. *Infrared and Raman spectroscopy: Principles and spectral interpretation* (Elsevier, 2017).

15. Rogalski, A. Recent progress in infrared detector technologies. *Infrared Physics & Technology* **54,** 136–154 (2011).

16. Tissot, J., Trouilleau, C., Fieque, B., Crastes, A. & Legras, O. Uncooled microbolometer detector: Recent developments at ULIS. *Opto-Electronics Review* **14,** 25–32 (2006).

17. Hu, H. *et al.* Far-field nanoscale infrared spectroscopy of vibrational fingerprints of molecules with graphene plasmons. *Nature Communications* **7,** 12334 (2016).

18. Ren, Z., Zhang, Z., Wei, J., Dong, B. & Lee, C. Wavelength-multiplexed hook nanoantennas for machine learning enabled mid-infrared spectroscopy. *Nature Communications* **13,** 3859 (2022).

19. Rodrigo, D. *et al.* Resolving molecule-specific information in dynamic lipid membrane processes with multi-resonant infrared metasurfaces. *Nature Communications* **9,** 2160 (2018).

20. Tittl, A. *et al.* Imaging-based molecular barcoding with pixelated dielectric metasurfaces. *Science* **360,** 1105–1109 (2018).

21. Leitis, A. *et al.* Angle-multiplexed all-dielectric metasurfaces for broadband molecular fingerprint retrieval. *Science Advances* **5,** eaaw2871 (2019).

22. Meng, J. *et al.* Compact chemical identifier based on plasmonic metasurface integrated with microbolometer array. *Laser & Photonics Reviews* **16,** 2100436 (2022).

23. Jeon, T. *et al.* Development of a compact and robust mid-infrared spectrometer by using a silicon/air hyperspectral filter. *ACS Photonics* **9,** 68–73 (2021).

24. Glassford, S. E., Byrne, B. & Kazarian, S. G. Recent applications of ATR FTIR spectroscopy and imaging to proteins. *Biochimica et Biophysica Acta (BBA)-Proteins and Proteomics* **1834,** 2849–2858 (2013).

25. Baker, M. J. *et al.* Using Fourier transform IR spectroscopy to analyze biological materials. *Nature Protocols* **9,** 1771–1791 (2014).

26. Morais, C. L., Lima, K. M., Singh, M. & Martin, F. L. Tutorial: Multivariate classification for vibrational spectroscopy in biological samples. *Nature Protocols* **15,** 2143–2162 (2020).

27. Taflove, A., Hagness, S. C. & Piket-May, M. Computational electromagnetics: the finite-difference time-domain method. *The Electrical Engineering Handbook* **3,** 15 (2005).

28. Oskooi, A. F. *et al.* MEEP: A flexible free-software package for electromagnetic simulations by the FDTD method. *Computer Physics Communications* **181,** 687–702 (2010).

Chapter 3

METHANE CONCENTRATION MEASUREMENTS USING TUNABLE DIODE LASER ABSORPTION SPECTROSCOPY

Methane is a major component of natural gas and a greenhouse gas with a global warming potential 28 times that of carbon dioxide. Although its atmospheric concentration is low (1.94 ppm) [1], it accounts for 11.1% of global warming [2]. A large fraction of methane emissions originates from agriculture and the energy industry. This motivates the development of scalable, cost-effective, rapid, and sensitive measurement systems. Conventionally, methane monitoring relies on infrared absorption spectroscopy sensors. Such sensors are widely used to detect methane leaks in industrial environments. However, sensitivity is limited because these systems use broadband incoherent light sources with narrowband filters [3–6].

Tunable diode laser absorption spectroscopy (TDLAS) has emerged as an alternative, offering high sensitivity and fast temporal response. By scanning and modulating the wavelength of distributed feedback (DFB) lasers across molecular absorption lines, a TDLAS system can quantify absorption. Wavelength modulation combined with lock-in detection rejects broadband noise and baseline drifts, further enhancing detection limits and measurement stability [7–9].

Beyond conventional single-pass configurations, remote measurements are possible. TDLAS systems have been mounted on drones to detect methane by analyzing light reflected from the ground [10–12]. Although fully remote sensing is feasible, reflected power from the ground is inherently limited. To address this, passive retroreflectors can be installed at remote locations to maximize returned signal. Light may be delivered to these retroreflectors via beam steering (e.g., galvanometer mirrors) or through optical fibers. This approach enables surveying multiple locations with a single source–detector pair. Moreover, because the remote assembly including retroreflectors is entirely passive, deployment in hazardous environments involves lower risk.

This chapter first develops the theoretical model linking the modulated TDLAS signal to methane concentration (Section 3.1). Two experimental systems are then implemented: a free-space setup in which a pair of galvanometer mirrors directs the beam (Section 3.2), and a fiber-optic system in which a single-mode fiber

delivers the light (Section 3.7). In both systems, retroreflectors return the beam to the detector. For the free-space setup, signal processing methods are described (Section 3.3), the optimal wavelength modulation amplitude for maximizing the second-harmonic response is determined (Section 3.4), and the limit of detection is measured (Section 3.5). Real-time, multi-point methane monitoring is demonstrated by alternating beam positions between two retroreflectors (Section 3.6). Finally, real-time concentration measurements are replicated in the fiber-optic configuration (Section 3.7).

3.1   Theory

The absorption spectrum of a molecule may be observed by scanning the laser center wavelength near an absorption line and recording the transmitted power. However, this approach has practical limitations. For example, source power may vary as the center wavelength changes. Because these measurements integrate signals across all optical frequencies without filtering, they are susceptible to broadband noise. In TDLAS implementation, a small sinusoidal modulation at frequency f_{mod}, much higher than the wavelength scan rate, is applied to enable lock-in detection. Lock-in detection selects signal components at the modulation frequency and its harmonics, rejecting noise at other frequencies.

Figure 3.1(a) shows an example of molecular transmittance. Consider sinusoidal modulation of the laser center wavelength around the points indicated as A and B, assuming constant optical power regardless of wavelength. When the laser wavelength oscillates around A, which lies outside the absorption line, transmitted power remains constant (Figure 3.1(b)) and no component appears at f_{mod} or $2f_{mod}$. If the modulation is centered at B, on the absorption line, transmitted power varies with wavelength. Each modulation cycle produces two cycles of transmitted power variation because the transmittance profile is symmetric about the absorption wavelength. Thus modulation at f_{mod} yields an output oscillation at $2f_{mod}$. The second harmonic component may be isolated by a lock-in amplifier in TDLAS measurements.

To model this principle, the laser wavelength $\lambda(t)$ is expressed as a slow linear scan plus a fast sinusoidal modulation at frequency f_{mod}:

$$\lambda(t) = \lambda_0 + s_{mod}t + a_{mod}\cos(2\pi f_{mod}t), \tag{3.1}$$

where t is time, λ_0 is the unmodulated center wavelength, s_{mod} is the scan rate, a_{mod} is the modulation amplitude and f_{mod} is the modulation frequency. The scan rate is much lower than the modulation rate ($s_{mod} \ll 2\pi f_{mod}a_{mod}$). Figure 3.2 illustrates
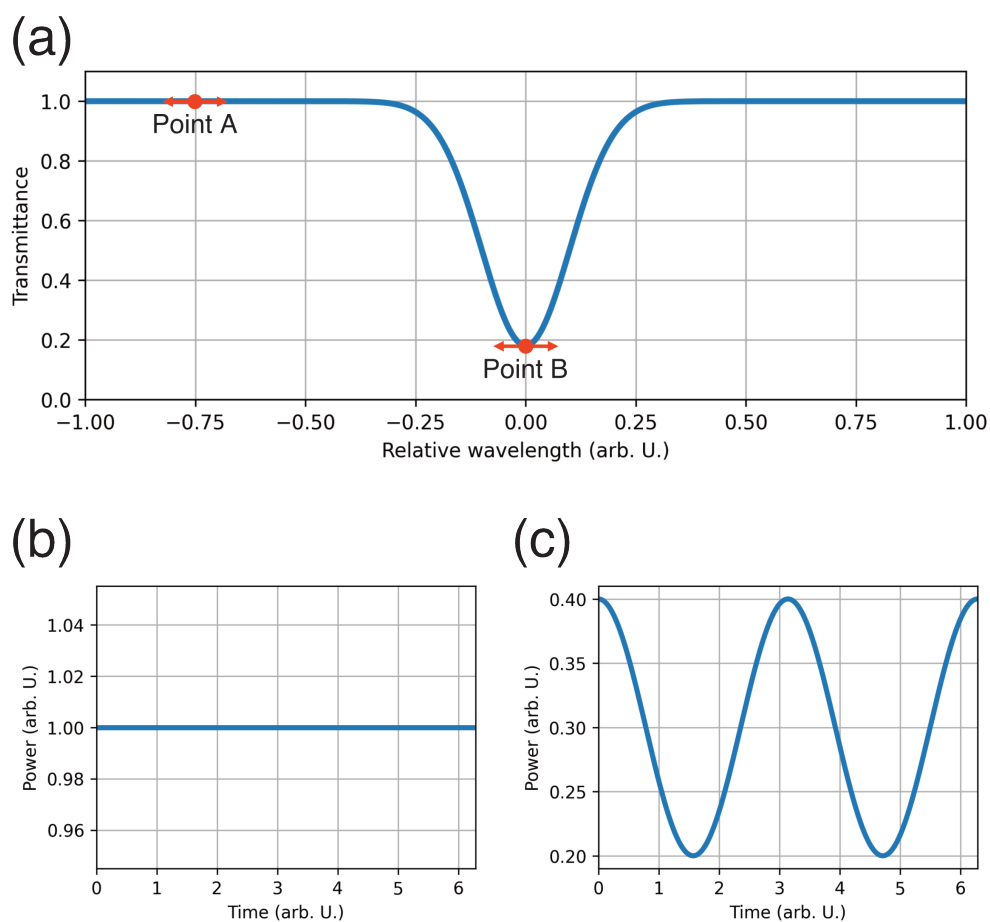
Figure 3.1: Graphical description of TDLAS principle. (a) Molecular transmittance near an absorption line. Laser wavelength is modulated sinusoidally around points A and B. (b) At point A, transmitted power remains constant because transmittance is flat. (c) At point B, within the absorption line, transmitted power varies with the center wavelength.

this wavelength modulation with $\lambda_0 = 0$ nm, $s_{mod} = 11.25$ nm/s, $a_{mod} = 0.188$ nm and $f_{mod} = 12.5$ kHz.

Assuming constant input power, independent of wavelength modulation, the input power may be expressed as:

$$P_i(\lambda) = P_i(t) = P_i. \tag{3.2}$$

The molar absorption spectrum may follow Lorentzian, Gaussian, or Voigt profiles depending on measurement conditions. The Lorentzian profile represents the intrinsic spectral shape. The Gaussian profile applies when Doppler broadening dominates, as at high temperature or low pressure. The Voigt profile is the convolution of Lorentzian and Gaussian profiles, representing intermediate cases [13]. Although the Voigt profile most accurately describes methane under the experimental conditions, only the Lorentzian profile is considered here for simplicity.

The lineshape function is denoted $L(\lambda)$. For a Lorentzian profile:

$$L(\lambda) = \frac{S}{\pi} \frac{\sigma/2}{(\lambda - \lambda_0)^2 + (\sigma/2)^2}, \tag{3.3}$$

where the spectrum is centered at wavelength λ_0, has full width at half maximum σ and line intensity S. Figure 3.2(b) illustrates this profile with $\sigma = 0.057$ nm.

Using the lineshape function and Beer's law, transmitted power through the gas is

$$P_o(\lambda) = P_i \exp\left[-c\, d\, L(\lambda)\right], \tag{3.4}$$

where c is the target molecule concentration and d is the optical path length. The product $c\, d$, or path integrated concentration, is commonly used as a figure of merit for TDLAS performance.

By substituting Equations 3.1 and 3.4, the time-domain output power becomes

$$P_o(t) = P_i \exp\left[-c\, d\, L\left(\lambda_0 + s_{mod}\, t + a_{mod} \cos(2\pi f_{mod} t)\right)\right]. \tag{3.5}$$

For a Lorentzian profile (Equation 3.3), this expression simplifies to

$$P_o(t) = P_i \exp\left[-\frac{c\, d\, S}{\pi} \frac{\sigma/2}{\left(s_{mod}\, t + a_{mod} \cos(2\pi f_{mod} t)\right)^2 + (\sigma/2)^2}\right]. \tag{3.6}$$

The photodetector voltage is

$$V_o(t) = r_{pd}\, P_o(t),$$
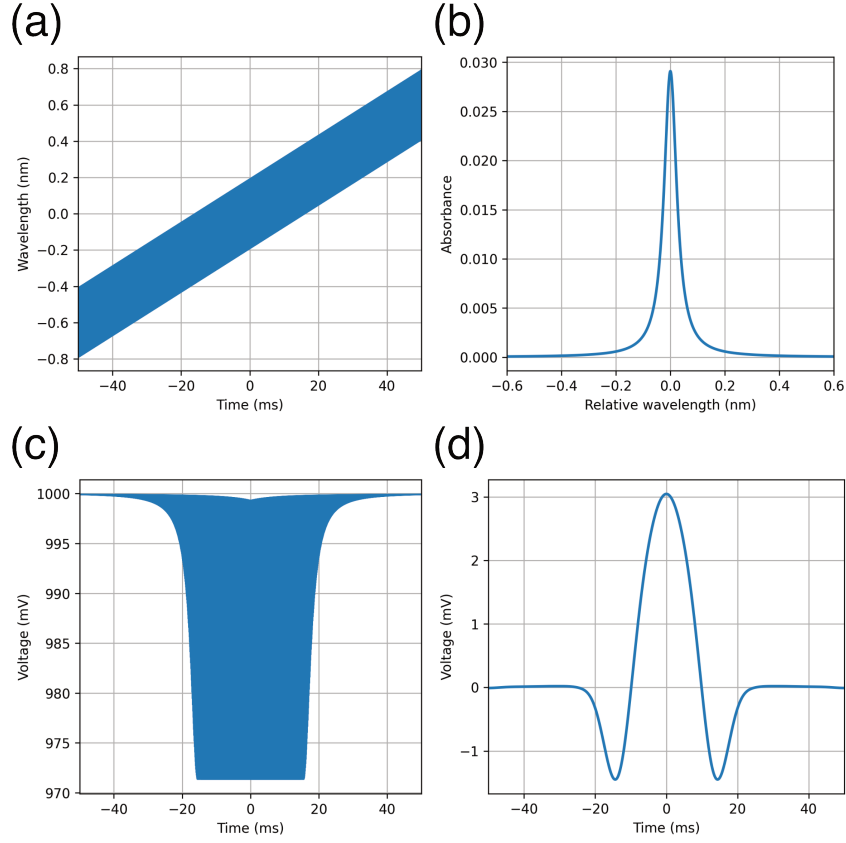
Figure 3.2: Theoretical description of TDLAS measurements. (a) Time-domain wavelength modulation showing a slow linear scan with superimposed sinusoidal oscillation. (b) Lorentzian absorption profile. (c) Simulated raw detector voltage. (d) Detector voltage demodulated at $f_{ref} = 2f_{mod}$.

where r_{pd} is the responsivity in volts per watt. Figure 3.2(c) presents the time-domain output voltage. The voltage fluctuation is most pronounced near the absorption peak (at $t = 0$).

Demodulation is performed by a lock in amplifier using a reference frequency f_{ref} and time constant τ. The time constant sets the cutoff frequency of the low-pass filter and is chosen so that $\tau \gg 1/(2\pi f_{mod})$ while remaining much smaller than the wavelength scan period. The demodulated signal $V_d(t)$ is

$$V_d(t) = \frac{1}{\tau} \int_{t-\tau}^{t} \sin\left(2\pi f_{ref}\, s + \phi\right) V_o(s)\, \mathrm{d}s, \tag{3.7}$$

where ϕ is the reference phase. To extract the second-harmonic component, f_{ref} is set to $2f_{mod}$, as shown in Figure 3.2(d).

3.2 TDLAS System with Free-space Light Delivery

The free-space optical setup for TDLAS measurements is shown in Figure 3.3. A distributed feedback laser (Model DFB1654, Thorlabs Inc.) operating at 1654 nm with 80 mW output serves as the light source. Two function generators (Model 33220A, Agilent Technologies) produce a 10 Hz ramp and a 12.5 kHz sinusoid. Their outputs are combined via a power combiner and applied to the laser driver to control wavelength modulation. The beam is collimated and directed to a 50:50 beam splitter. A pair of galvanometer mirrors (Model GVS002, Thorlabs Inc.) alternately steers the beam to two retroreflectors located 4 m from the steering mirrors. A gas cell with wedged CaF_2 windows and 0.1 m physical length provides a 0.2 m path through methane. Reflected light returns through the beam splitter and is focused onto a germanium photodiode (Model PDA30B2, Thorlabs Inc.). The photodiode output is fed to a lock-in amplifier (Model SR810, Stanford Research Systems) and demodulated at the first harmonic (12.5 kHz) for baseline measurement or the second harmonic (25.0 kHz) for methane detection. The demodulated signal is digitized by a data acquisition board (PCI-6221, National Instruments) and recorded using a custom MATLAB script.

3.3 Signal Processing

Figure 3.4(a) shows an example of the photodetector output voltage. The combination of the slow wavelength scan (s_{mod} in Equation 3.1) and the fast sinusoidal modulation at f_{mod} (a_{mod} in Equation 3.1) produces a raw signal that appears noisy but contains frequency components at f_{mod}, $2f_{mod}$ and higher harmonics, as seen in the Fourier transform in Figure 3.4(b).

The raw voltage is processed by a lock-in amplifier. Using a reference signal, the amplifier demodulates the photodetector output and applies a low pass filter. The filter cutoff frequency is set by the time constant τ. This cutoff must lie below the reference frequency (either f_{mod} or $2f_{mod}$) yet above the wavelength scan rate. In the present experiment, $f_{mod} = 12.5$ kHz and the scan rate is 10 Hz. Therefore, τ is chosen as 1 ms, which corresponds to a cutoff frequency of 159 Hz.

To detect methane absorption, the reference frequency is set to $2f_{mod} = 25.0$ kHz. Because the center wavelength is scanned, the amplifier output versus time corresponds directly to center wavelength. Figure 3.4(c) shows the demodulated output over a 100 ms scan, with the top axis indicating the change in center wavelength $\Delta\lambda$. In the presence of methane, a peak appears. The amplitude of this peak, called the
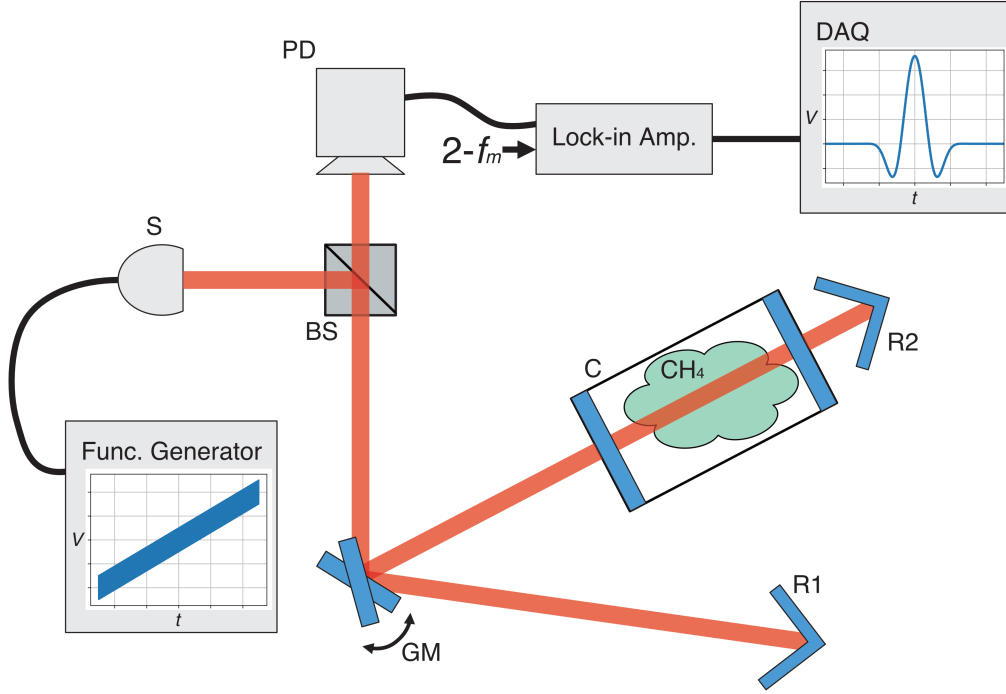
Figure 3.3: Setup of the TDLAS system with free space light delivery. S denotes light source; PD photodiode; BS beam splitter; GM galvanometer mirrors; C gas cell with 0.1 m optical path; R1 and R2 retroreflectors. Retroreflectors are 4 m from GM and the cell is placed before R2 to introduce CH_4 flow.

2-f signal, is defined as the difference between its maximum and its minimum.

Similarly, the photodetector output may be demodulated at $f_{mod} = 12.5$ kHz. In this case, the output voltage is proportional to the incident optical power and thus serves as a measure of system input power. This is useful since the 2-f signal amplitude is proportional to input power (Equation 3.4).

3.4 Optimal Modulation Amplitude for Methane Detection

One of the important parameters of this system is the modulation amplitude a_{mod} in Equation 3.1. It describes how much modulation in the frequency of f_{mod}. To test influence of a_{mod} in 2-f signal, signal is measured with various a_{mod} while the gas concentration within the cell is fixed to 10,000 ppm. The modulation amplitude from the function generator is changed from 50 mV to 500 mV with 25 mV steps. This gives rise to the wavelength modulation a_{mod} from 0.0325 nm to 0.325 nm with 0.01875 nm steps. The gas concentration within the gas cell was maintained at 2,000 ppm-m (10,000 ppm) by continuously flowing 10,000 ppm CH_4 (AirGas Inc.) at 10.0 sccm. To stabilize the concentration, the measurements were conducted after
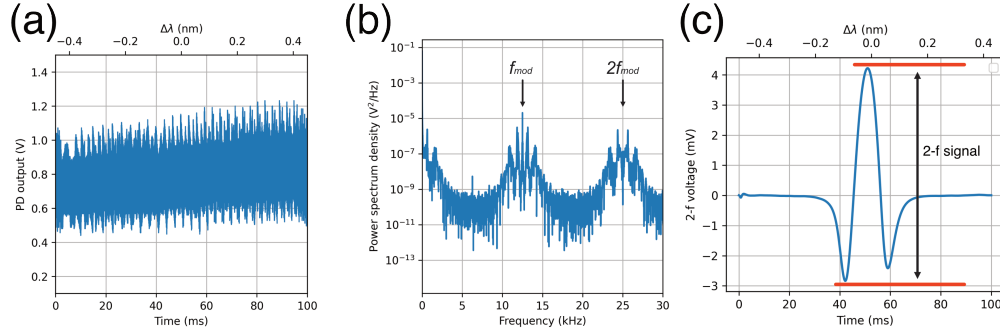
Figure 3.4: Data processing for $2f_{mod}$ signal. (a) Raw photodiode signal. (b) Fourier transform of the raw signal showing components at the modulation frequency f_{mod} and its second harmonic. (c) Lock-in amplifier output. The two-f signal is defined as the difference between the red-marked maximum and minimum of the demodulated voltage. In panels (a) and (c), the lower horizontal axis is time and the upper axis denotes the change in center wavelength $\Delta\lambda$ relative to the wavelength at 50 ms.

5 minutes of gas flow. The lock-in amplifier's time constant is set to 1 ms (equivalent to the cut-off frequency of 159 Hz). At each a_{mod}, the output signal is recorded 100 times at a sampling rate of 10 kHz.

Figure 3.5(a) shows raw outputs for three values of a_{mod}. Peak amplitude and width vary with a_{mod}. The average second harmonic signal (at $2f_{mod}$) is plotted as a function of a_{mod} in Figure 3.5(b) and compared to the model in Section 3.1. The model second harmonic response was calculated using Equations 3.4 and 3.7. Three parameters were adjusted by least squares fitting to the experimental data: input power equivalent voltage V_i, the product cdS, and the linewidth σ. Fitting yields $V_i = 26.44$ V, $cdS = 0.27$ nm and $\sigma = 0.13$ nm. The second harmonic signal is maximized at $a_{mod} = 0.25$ nm. All subsequent measurements use this modulation amplitude.

3.5 Limit of Detection Measurement

Next, the limit of detection is evaluated. Beer's law indicates that attenuation depends on path length and concentration. Consequently, detection limit is expressed in ppm-m by the product of concentration and path length. In these measurements, the path length is fixed at 0.2 m, since the beam traverses the 0.1 m gas cell twice.

The optical setup is shown in Figure 3.3. A retroreflector is positioned 4 m from the galvanometer mirrors. A gas cell is installed before one retroreflector (R2) and connected to mass flow controllers (MFCs, MKS Instruments) to set methane concentration. One MFC supplies 10,000 ppm CH_4 and two MFCs regulate argon
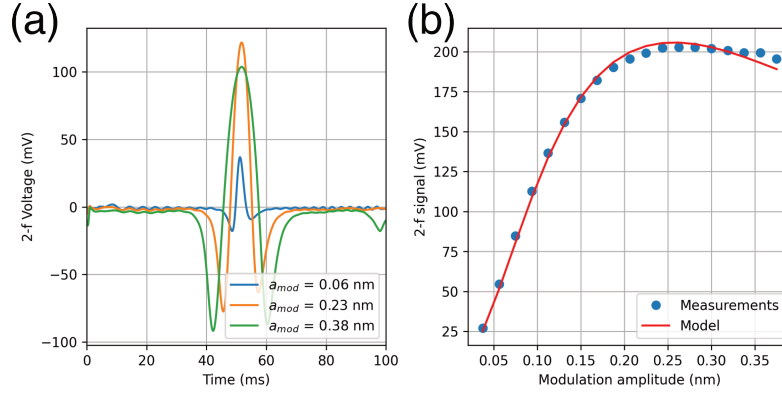
Figure 3.5: Measurement of optimal modulation amplitude. (a) 2-f voltage outputs at modulation amplitudes a_{mod} = 0.06 nm, 0.23 nm, and 0.38 nm. (b) Measured $2f_{mod}$ signal outputs at 2000 ppm-m CH_4 concentration (blue), and predictions from the numerical model (red) at various modulation amplitudes a_{mod}.

flow. Gas flow is allowed to stabilize for five minutes before measurement. Concentration is varied between 0 ppm-m (0 ppm) and 93.6 ppm-m (468 ppm). At each concentration, the 2-f signal is recorded 100 times.

Figure 3.6(a) presents lock-in amplifier outputs at four concentrations from 0 ppm-m to 20 ppm-m. The peak near 50 ms scales with methane concentration. All 2-f signals are extracted and plotted against CH_4 concentration in Figure 3.6(b). Assuming linearity, a linear regression yields a responsivity of 0.107 mV/ppm-m. The system noise A_{noise} is defined as the standard deviation of the 2-f signal at 0 ppm-m, measured as 0.0178 mV. The detection limit, defined at a signal-to-noise ratio of three, is therefore

$$\text{LoD} = \frac{3\,A_{\text{noise}}}{\text{responsivity}} = 0.501 \text{ ppm-m.}$$

3.6 Real-time Monitoring of Gas Concentration

Real-time monitoring of methane concentration is demonstrated using the free-space system with two retroreflectors positioned 4 m from the galvanometer mirrors and the gas cell placed before one reflector. Retroreflector positions are identified by scanning the mirrors while recording first-harmonic reflectance. The beam is rastered horizontally from 0.6° to 2.2° and vertically from -6.2° to -7.0° in 0.005° increments. Figure 3.7(a) shows the setup with both retroreflectors in place (gas cell removed for this photograph). The scan result in Figure 3.7(b) reveals two reflectance peaks corresponding to the retroreflectors. Differences in peak amplitude reflect differences in reflector surface properties. Cross-sections in Figure 3.7(c) indicate mirror
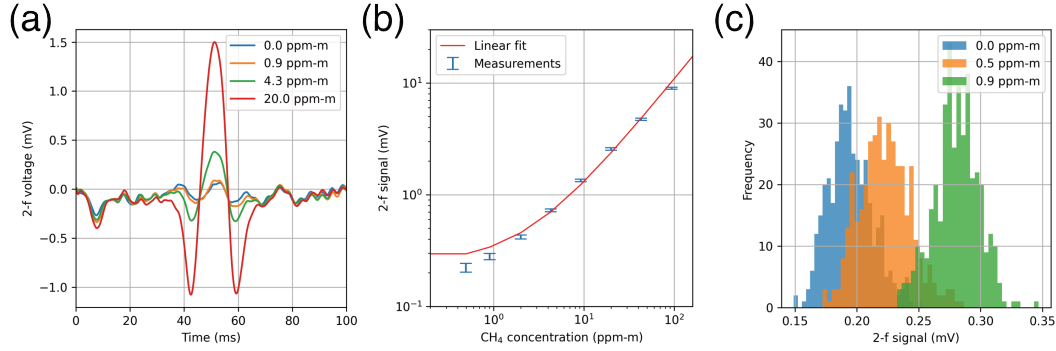
Figure 3.6: Limit of detection measurements. (a) Raw lock-in amplifier outputs for path-integrated concentrations from 0 to 20 ppm-m. (b) 2-f signal amplitude versus concentration from 0 to 93.6 ppm-m. Linear regression yields a responsivity of 0.11 mV/ppm-m. (c) Histograms of 2-f signal amplitudes from 400 measurements at 0.0 ppm-m (blue), 0.5 ppm-m (orange) and 0.9 ppm-m (green).

deflection angles of (0.87°, -6.55°) for position 1 and (1.89°, -6.60°) for position 2. Mirror rotation is half these deflection angles due to the two-way beam path.

For real-time monitoring, the beam was alternately directed to two positions. Measurements at each position were acquired at approximately 1 Hz. The first-harmonic signal at both positions was recorded for 300 s to evaluate system repeatability, as shown in Figure 3.8(a).

Next, the gas concentration in the cell was varied over 30 minutes. Pure argon flowed from 0 to 180 s. Methane flow of 1,000 ppm was introduced from 180 to 800 s, producing a path integrated concentration of 200 ppm-m. Between 800 and 1,200 s, methane concentration was reduced to 500 ppm (100 ppm-m). After 1,200 s, methane flow was stopped. The second harmonic signal was recorded at both positions for 1,800 s at 1 Hz per position. Figure 3.8(b) shows that only position 2, which includes the gas cell, exhibits an increase in the 2-f signal; Position 1 remains at baseline. Methane concentration changes are tracked in real time. A delay between the indicated concentration intervals and the signal response reflects the six meter long tubing between the mass flow controllers and the cell.

3.7 TDLAS System with Fiber-optic Light Delivery

A TDLAS system using fiber optic delivery is illustrated in Figure 3.9. This configuration reuses the laser, function generators, photodetector and readout electronics from the free-space setup. A fiber optic circulator replaces the collimator, beam splitter and focusing lens. Light is transmitted through a 50 m single-mode fiber
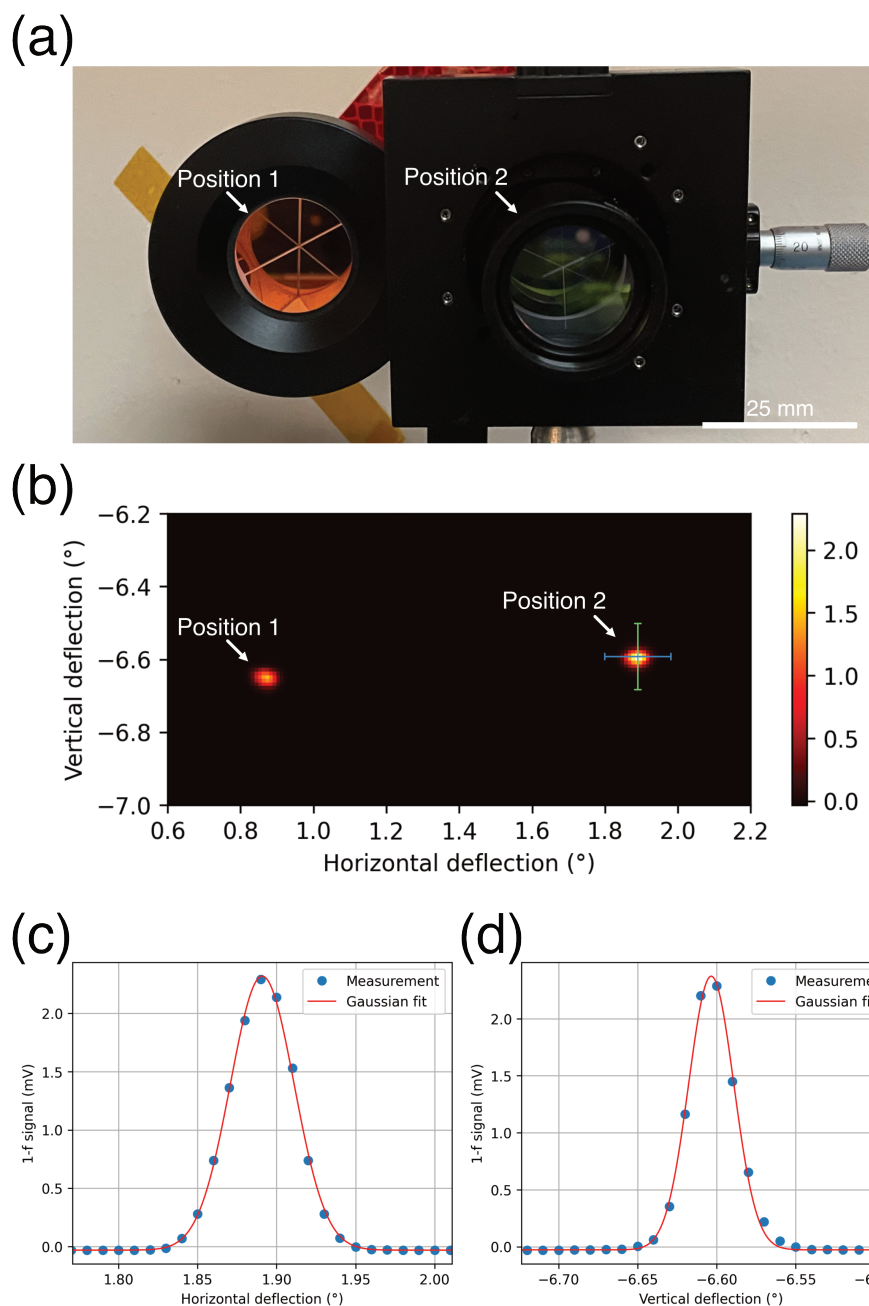
Figure 3.7: Retroreflector location via galvanometer scan. (a) Photograph of the setup showing retroreflectors 4 m from the galvanometer mirrors. (b) First-harmonic reflectance versus mirror deflection angle showing two peaks at the retroreflector positions. (c) Horizontal cross section along the blue line in panel b, corresponding to position 1. Gaussian fit yields a full width at half maximum of 0.047°. (d) Horizontal cross section along the green line in panel b, corresponding to position 2. Gaussian fit yields a full width at half maximum of 0.033°.

Figure 3.8: Real-time measurements at two retroreflector locations. Position 1 did not include a gas cell; position 2 included the gas cell. (a) Reflectance versus time over 300 s. (b) Second harmonic signal versus tim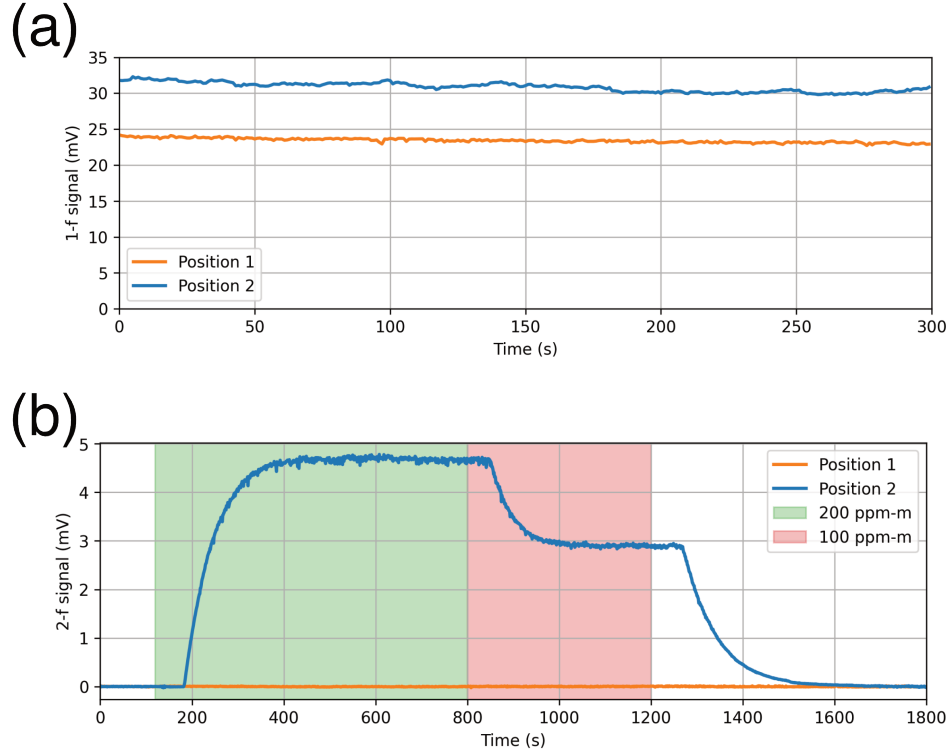e. Shaded regions indicate periods when 1,000 ppm and 500 ppm methane were introduced, corresponding to path integrated concentrations of 200 ppm-m and 100 ppm-m.

and collimated by a lens. The collimated beam passes through a gas cell, reflects from a retroreflector and is recoupled into the fiber by the same lens. The return signal is routed by the circulator to the photodetector.

The real-time measurement of methane concentration was performed at 1 Hz. The first-harmonic signal was recorded over 300 s to track reflected power, as shown in Figure 3.10(a).

Gas concentration in the cell was then varied over 30 min. Pure argon flowed from 0 to 200 s. Methane at 500 ppm was introduced from 200 to 800 s, yielding a path integrated concentration of 100 ppm-m. From 800 to 1,200 s, methane concentration was increased to 1,000 ppm (200 ppm-m). After 1,200 s, methane flow was stopped. Figure 3.10(b) presents the second harmonic signal over 1,800 s, demonstrating real-time tracking of gas concentration.
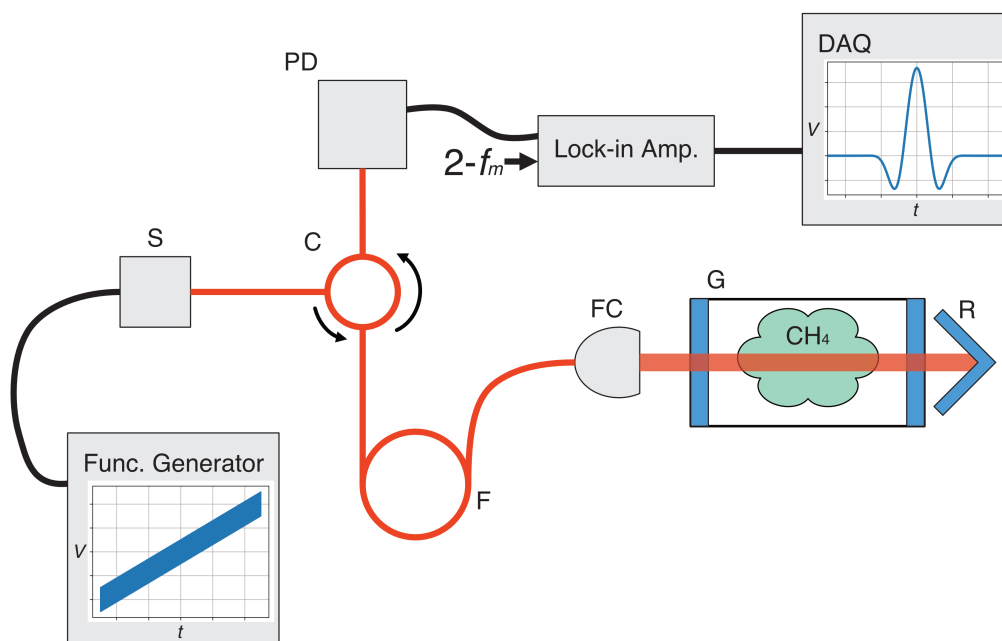
Figure 3.9: Setup of the TDLAS system with light delivery through optical fibers. S light source; PD photodiode; C circulator; F 50 m single-mode fiber; FC fiber collimator; G gas cell (0.1 m); R retroreflector.

3.8 Conclusion

This chapter presented a tunable diode laser absorption spectroscopy system. A theoretical model relating gas concentration to the second-harmonic signal was first derived. Two experimental configurations were implemented. In the free-space system, galvanometer mirrors directed the beam to remote retroreflectors. Modulation amplitude was optimized, the limit of detection was determined, and real-time methane concentration was measured at two reflector positions. In the fiber-optic system, a 50 m single-mode fiber delivered light to a retroreflector, and real-time concentration measurements were similarly demonstrated.

A limitation of the current system is calibration's dependence on input power. Although Section 3.5 reports a responsivity measurement, it relies on reflected power. Concurrent measurement of reflected power (first harmonic) would enable absolute calibration but was not feasible with the single-channel lock-in amplifier used here.

Although only methane was measured in this study, other gases may be targeted by selecting appropriate lasers. For example, ammonia is probed at 1,530 nm,
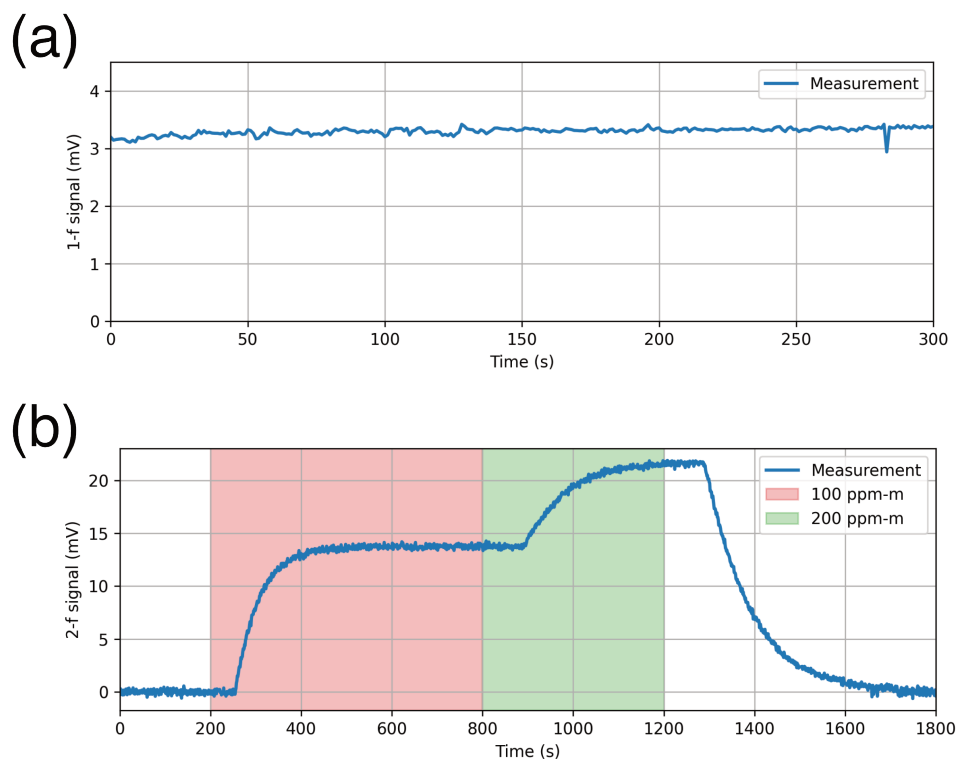
Figure 3.10: Real-time measurements from a single retroreflector via a 50 m single-mode fiber. (a) First-harmonic reflectance over 300 s. (b) Second-harmonic signal over 1,800 s. Shaded regions indicate periods when 500 ppm and 1,000 ppm methane were introduced, corresponding to path integrated concentrations of 100 ppm-m and 200 ppm-m, respectively.

while carbon monoxide, carbon dioxide and hydrogen sulfide absorb near 1,580 nm. These species could be integrated into the existing system using the same detector and optical components.

The ability to monitor multiple locations with a single source–detector pair, either by scanning galvanometer mirrors or by switching among fibers, offers significant cost reduction for multi-site or multi-species gas monitoring. Because retroreflectors are inexpensive to manufacture, this approach could substantially lower the cost of large-scale environmental gas monitoring and support greenhouse gas reduction efforts.

Reference

1. Thoning, K., Dlugokencky, E., Lan, X. & NOAA Global Monitoring Laboratory. *Trends in globally-averaged CH4, N2O, and SF6* 2022.

2. Agency, U. E. P. *Importance of methane* U.S. EPA. `https://www.epa.gov/gmi/importance-methane` (2025).

3. Dinh, T.-V., Choi, I.-Y., Son, Y.-S. & Kim, J.-C. A review on non-dispersive infrared gas sensors: Improvement of sensor detection limit and interference correction. *Sensors and Actuators B: Chemical* **231,** 529–538 (2016).

4. Zhu, Z., Xu, Y. & Jiang, B. A one ppm NDIR methane gas sensor with single frequency filter denoising algorithm. *Sensors* **12,** 12729–12740 (2012).

5. Kwaśny, M. & Bombalska, A. Optical methods of methane detection. *Sensors* **23,** 2834 (2023).

6. Hodgkinson, J. & Tatam, R. P. Optical gas sensing: A review. *Measurement Science and Technology* **24,** 012004 (2013).

7. Zhang, Z., Li, M., Guo, J., Du, B. & Zheng, R. A portable tunable diode laser absorption spectroscopy system for dissolved CO2 detection using a high-efficiency headspace equilibrator. *Sensors* **21,** 1723 (2021).

8. Werle, P., Mücke, R. & Slemr, F. The limits of signal averaging in atmospheric trace-gas monitoring by tunable diode-laser absorption spectroscopy (TDLAS). *Applied Physics B Photophysics and Laser Chemistry* **57,** 131–139 (1993).

9. Zhimin, P., Yanjun, D., Lu, C., Xiaohang, L. & Kangjie, Z. Calibration-free wavelength modulated TDLAS under high absorbance conditions. *Optics Express* **19,** 23104 (2011).

10. Iwaszenko, S., Kalisz, P., Słota, M. & Rudzki, A. Detection of natural gas leakages using a laser-based methane sensor and UAV. *Remote Sensing* **13,** 510 (2021).

11. Corbett, A. & Smith, B. A study of a miniature TDLAS system onboard two unmanned aircraft to independently quantify methane emissions from oil and gas production assets and other industrial emitters. *Atmosphere* **13,** 804 (2022).

12. Lu, H. *et al.* A remote sensor system nased on TDLAS technique for ammonia leakage monitoring. *Sensors* **21,** 2448 (2021).

13. Armstrong, B. Spectrum line profiles: The Voigt function. *Journal of Quantitative Spectroscopy and Radiative Transfer* **7,** 61–88 (1967).

Chapter 4

MEASUREMENT OF THE CONDUCTANCE IN SOLID STATE NANOPORES

The detection mechanisms of biological olfactory systems and nanopore-based sensors exhibit notable similarities. Both rely on changes in ionic conductivity across a membrane to detect and distinguish analytes. In olfaction, ionic signals within sensory neurons trigger neural responses; in nanopore sensors, ionic current modulations are detected for analysis.

Nanopore-based DNA sequencing represents a particularly successful application of this technology. In this method, DNA molecules translocate through a nanopore in a lipid bilayer membrane, producing characteristic disruptions in ionic current. Each nucleotide (adenine, guanine, thymine or cytosine) generates a distinct current signature, enabling base identification. Traditional sequencing techniques, such as sequencing by synthesis, copies DNA strands one nucleotide at a time. Nanopore sequencing, by contrast, reads long DNA fragments (exceeding 100 kilobase pairs) directly, reducing the requirement for sample amplification and simplifying the overall workflow.

Biological nanopores derived from pore-forming proteins like α-hemolysin have proven effective in DNA sequencing. They provide precise dimensions and structural uniformity, which support consistent device performance. Sequencing platforms using α-hemolysin achieve pore diameters of about 1.5 nm. Genetic engineering enables customization of these nanopores for specific sequencing requirements or for analysis of larger analytes, such as double-stranded DNA. Some commercial platforms employ a protein motor to slow DNA translocation and improve base-call accuracy.

Despite their strengths, biological nanopores also have limitations. Sequencing devices exhibit relatively low pore density. Sensitivity to environmental parameters, including pH and the maximum applied potential across the pore, can affect performance. Maintaining lipid bilayers and pore proteins over time requires controlled environments and stable operating conditions to ensure device longevity.

Solid state nanopores provide an alternative approach, fabricated by microfabrication and semiconductor processing techniques. Common materials include dielectric
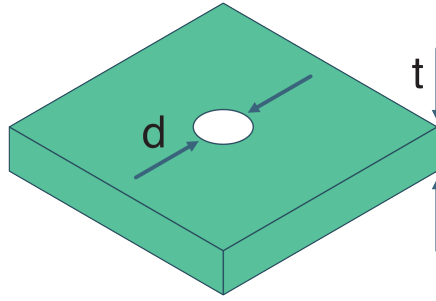
Figure 4.1: Geometry of a cylindrical nanopore with diameter d in a membrane of thickness t.

membranes such as silicon nitride (SiN_x), silicon dioxide (SiO_2) and hafnium dioxide (HfO_2) as well as two dimensional materials such as molybdenum disulfide (MoS_2) and graphene. Solid state nanopores offer mechanical stability, compatibility with integrated electronics and improved operational robustness compared to biological pores. They may also incorporate embedded electrodes to slow DNA translocation and improve detection accuracy.

Solid state nanopores also present challenges. Achieving pore diameters below a few nanometres with uniformity is difficult and precise control of surface chemistry remains complex. Lithographic resolution limits and processing variability impose constraints on minimum pore size.

Despite fabrication challenges, pore geometry remains the key factor governing sensor performance. The conductance of a nanopore depends primarily on geometric parameters such as diameter, thickness and shape. Understanding these dependencies provides design guidance for nanopore devices and associated measurement systems. This chapter presents analytical and numerical models of nanopore conductance and compares their predictions to experimental measurements from nanopores with varying diameters. The following chapter introduces a design and measurement approach aimed at increasing nanopore detector throughput.

4.1 Analytical Model of the Nanopore Conductance

Consider a cylindrical nanopore as shown in Figure 4.1. The pore's conducting region is an electrolyte-filled cylinder. The channel conductance is

$$G_{channel} = \frac{1}{R_{channel}} = \sigma \frac{\pi d^2}{4t},$$

(4.1)

where $R_{channel}$ is the channel resistance, σ is the electrolyte conductivity, d is the pore diameter and t is the membrane thickness.

For thin membranes, ion transport from the bulk electrolyte to the pore entrance contributes significantly to the total resistance. Hall first derived the access conductance as [1]

$$G_{access} = \frac{1}{R_{access}} = 2\sigma d, \tag{4.2}$$

where R_{access} is the access resistance. Access conductance depends only on pore diameter and is independent of membrane thickness.

Combining channel and access contributions, the total conductance is

$$G_{total} = \left(G_{channel}^{-1} + 2\,G_{access}^{-1}\right)^{-1} = \sigma \left(\tfrac{4t}{\pi d^2} + \tfrac{1}{d}\right)^{-1}. \tag{4.3}$$

The factor of two on the access term accounts for both pore entrances.

From the analytical model, two observations follow. First, for very thin membranes ($t \rightarrow 0$), conductance is dominated by access conductance, yielding $G_{total} \approx 2\,G_{access}$. Second, when pore diameter is much smaller than membrane thickness ($d \ll t$), channel conductance dominates, so $G_{total} \approx G_{channel}$.

4.2 Numerical Model of the Nanopore Conductance

The analytical model offers clear scaling relations but cannot capture irregular pore geometries, ionic interactions or the presence of translocating particles. To address these limitations, a numerical model was implemented in COMSOL Multiphysics®. The Secondary Current Distribution interface in the Electrochemistry Module solves for ionic current and potential distribution in an electrolyte bath with silver chloride reference electrodes at both ends. A constant 0.1 V bias is applied between electrodes, and the resulting current through one electrode is recorded. The electrolyte is potassium chloride with conductivity $\sigma = 19.9859$ S/m, matching experimental conditions.

For computational efficiency, a 2-D axisymmetric geometry is used (Figure 4.2(a)). The model comprises a nanopore of diameter d in a membrane of thickness t, surrounded by an electrolyte domain of diameter ϕ_{sim} and height h_{sim}. Top and bottom boundaries serve as electrodes; all other boundaries are insulating.

The effect of simulation domain size was assessed by varying the electrolyte bath diameter ϕ_{sim} from 100 μm to 5,000 μm while computing current through a 200 nm diameter pore in a 50 nm thick membrane. As shown in Figure 4.2(b), the
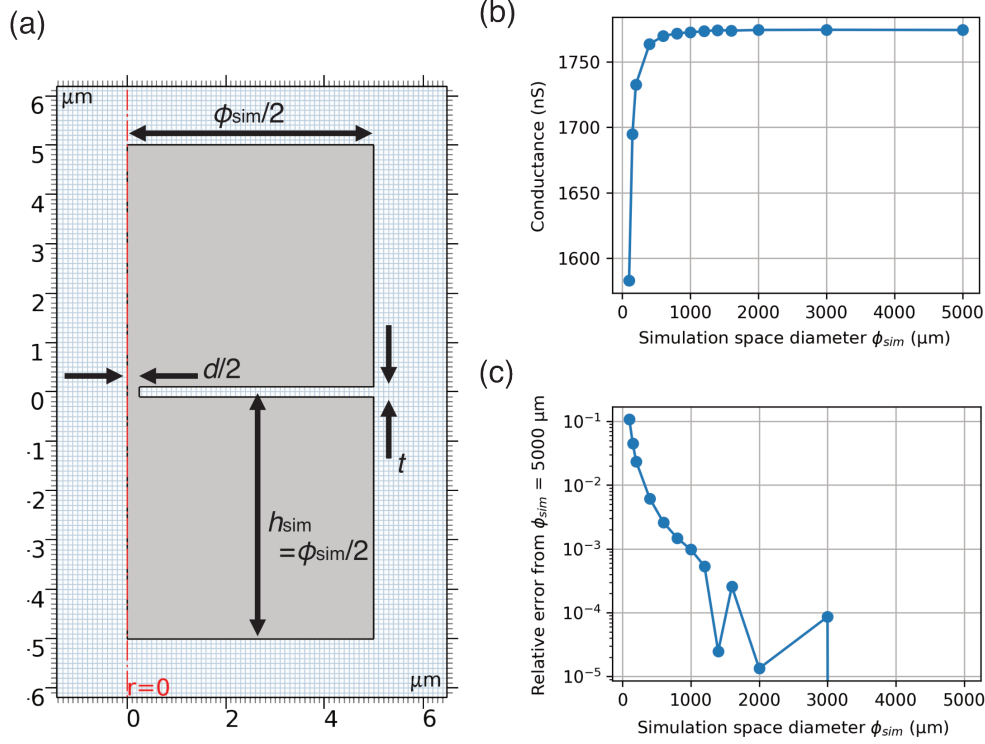
Figure 4.2: Effect of simulation domain size on conductance accuracy. (a) COMSOL simulation geometry showing the axisymmetric domain. The red dashed line at $r = 0$ is the cylindrical axis. (b) Simulated conductance of a 200 nm diameter nanopore as a function of simulation domain diameter ϕ_{sim}. (c) Relative error in conductance compared to the $\phi_{\text{sim}} = 5000\ \mu$m case.

simulated conductance converges with increasing domain size. A relative error analysis in Figure 4.2(c) shows that $\phi_{\text{sim}} =$1,000 µm yields results within 0.1% of the $\phi_{\text{sim}} =$5,000 µm reference. Computational cost remains stable because COMSOL employs adaptive meshing.

Figure 4.3 shows the electrolyte potential distribution around a 2,000 nm diameter nanopore in a 200 nm thick membrane under a 1.0 V applied bias. Gray arrows indicate ionic current flow. Most of the potential drop occurs near the nanopore, reflecting its low conductance. Because the drop extends beyond the pore channel, access resistance makes a significant contribution to the total conductance.

The analytical models were compared to numerical simulations to verify behavior in extreme regimes (thin membrane $t \rightarrow 0$ and small pore $d \ll t$). First, conductance of 500 nm diameter nanopores was simulated for membrane thicknesses from 2 nm to 10 µm. Figure 4.4(a) plots the simulated conductance alongside analytical
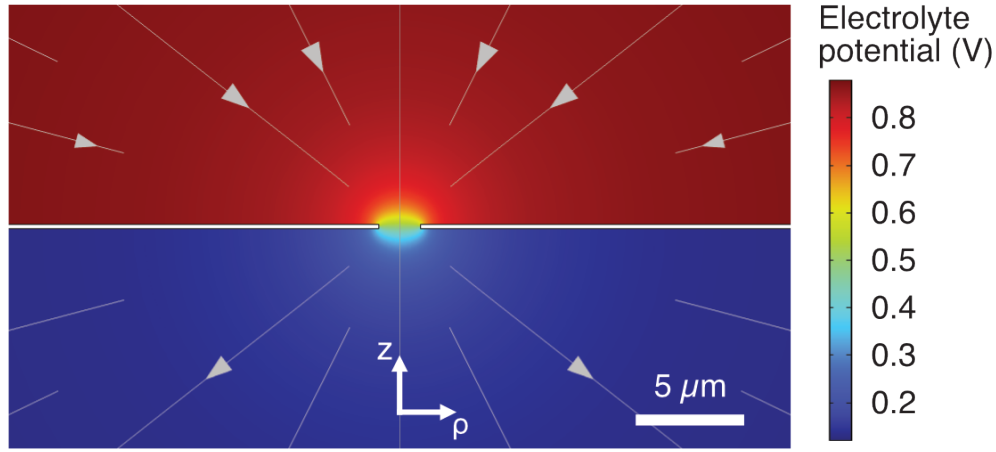
Figure 4.3: Simulated electrolyte potential distribution around a nanopore of diameter 2,000 nm. Gray arrows indicate ionic current flow. Data are shown in the ρz plane of cylindrical coordinates.
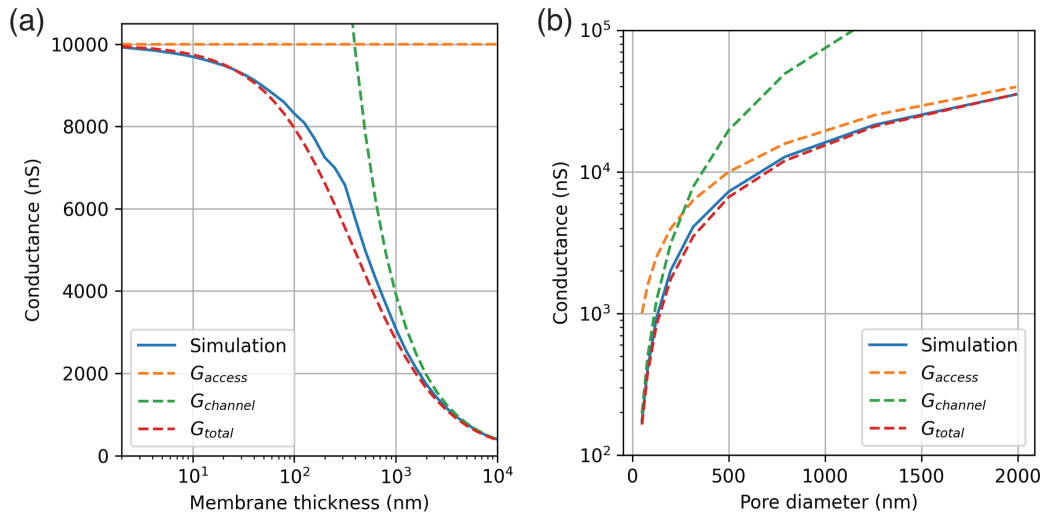

Figure 4.4: Comparison of numerical and analytical conductance models. (a) Simulated conductance of a 500 nm diameter nanopore as a function of membrane thickness (solid blue). (b) Simulated conductance of nanopores in a 200 nm thick membrane as a function of diameter (solid blue). Analytical access conductance G_{access} (dashed orange), channel conductance G_{channel} (dashed green) and total conductance G_{total} (dashed red) are calculated from Equations 4.2, 4.1 and 4.3.
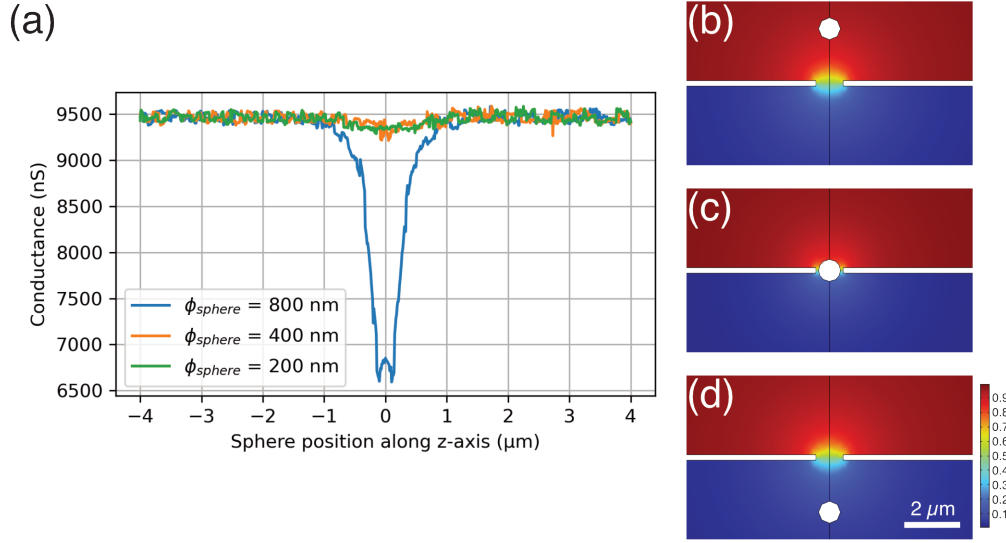
Figure 4.5: Conductance of a nanopore with a sphere at various positions. (a) Simulated conductance of a 1000 nm diameter nanopore with a sphere at varying axial positions. (b) Electrolyte potential distribution around the nanopore with an 800 nm diameter sphere positioned at +2 μm. (c) Distribution with the sphere at 0 μm. (d) Distribution with the sphere at –2 μm. Sphere position indicates distance from the membrane center.

predictions. The total conductance model (Equation 4.3) agrees with simulation across the full thickness range. In contrast, the access conductance model (Equation 4.2) is accurate only for membranes thinner than 10 nm, and the channel conductance model (Equation 4.1) applies only for thicknesses greater than 1 μm. These results confirm the limiting-case observations.

Next, with membrane thickness fixed at 200 nm, pore diameter was varied from 10 nm to 1.2 μm. Figure 4.4(b) shows that the total conductance model again reproduces the simulation trend. In the limit $d \ll t$, the channel conductance term dominates the total conductance.

Numerical models capture complex geometries and interactions beyond the scope of analytical models. Solid-state nanopore sensors detect particles by recording conductance changes during translocation. As a particle passes through the pore, it partially obstructs the channel, reducing conductance.

For the translocation simulation, a 1,000 nm diameter nanopore in a 200 nm thick membrane is centered at $z = 0$ μm. A silicon dioxide sphere is moved axially from $z = +3$ μm to $z = -3$ μm. Conductance is computed at each position for sphere diameters of 200 nm, 400 nm and 800 nm. Figure 4.5(a) plots conductance

versus sphere position and shows that the conductance decrease is not proportional to sphere size. Figures 4.5(b–d) present electrolyte potential distributions for an 800 nm sphere at $z = +2$ µm, 0 µm and -2 µm, respectively.

4.3   Experimental Method

Silicon nitride membranes were fabricated on silicon wafers coated with 50 nm of low-stress silicon nitride deposited by low-pressure chemical vapor deposition (LPCVD, Rogue Valley Microdevices). A silicon nitride hard mask was patterned by photolithography (MA/BA6, SUSS MicroTec) and transferred by plasma etching (see Appendix A). The bulk silicon substrate was removed by wet etching in hot KOH (see Appendix B), yielding a suspended membrane. Ellipsometry (M-2000, J.A. Woollam) measured the final membrane thickness as 45.6 nm. A single nanopore per chip, with diameters ranging from 60 nm to 472 nm, was milled by gallium ion beam (Nova 600, Thermo Fisher). Pore diameters were determined from scanning electron micrographs (Figure 4.7).

A conductivity standard solution (Cole-Parmer) of 19.9859 S/m was used as the electrolyte to eliminate uncertainty in solution conductivity. Samples were treated with O_2 plasma prior to measurement to improve wetting. The measurement configuration is shown in Figure 4.6. The chip was floated on the electrolyte bath to immerse the membrane underside. A 20 µL droplet of electrolyte was placed on the membrane top. Silver chloride electrodes (Cole-Parmer) contacted the bath and the droplet. The electrodes were connected to a SourceMeter 2400 (Keithley) for electrical characterization. Nanopore conductance was measured by applying DC voltages from -200 mV to $+200$ mV and recording the resulting currents.

4.4   Results and Discussion

Figure 4.7(a–d) shows examples of nanopores fabricated in silicon nitride membranes, with diameters ranging from 60 nm to 1,160 nm. The pore rims appear brighter due to redeposition of silicon nitride during milling. Pore morphology reflects the ion beam profile: small pores may appear elongated when the beam exhibits astigmatism, as in Figure 4.7(c). For larger pores, beam steering dominates the shape because the spot size remains below 100 nm. With a well-focused beam, even the smallest pores are circular, as in Figure 4.7(d).

Conductance was measured for five pores with diameters ranging from 60 nm to 472 nm. Figure 4.8 shows current versus voltage data for each pore. Linear regression of each data set yielded the conductance values. Figure 4.9 summarizes these
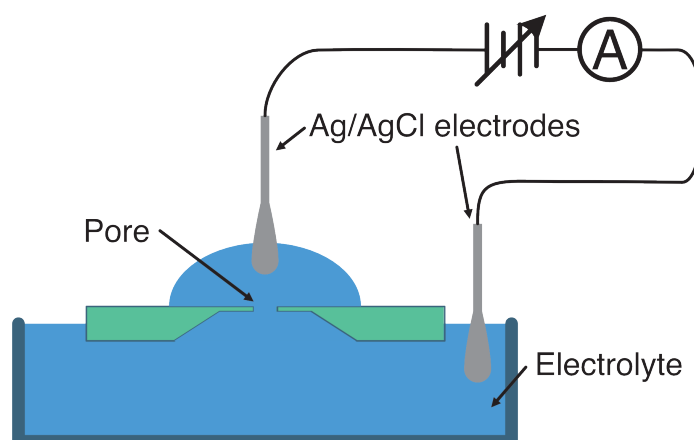
Figure 4.6: Conductance measurement setup. A silicon nitride chip containing a nanopore is floated on an electrolyte bath, and a droplet of electrolyte is placed on the membrane top. Ag/AgCl electrodes contact the bath and the droplet to complete the circuit. A variable DC voltage is applied while current is recorded.
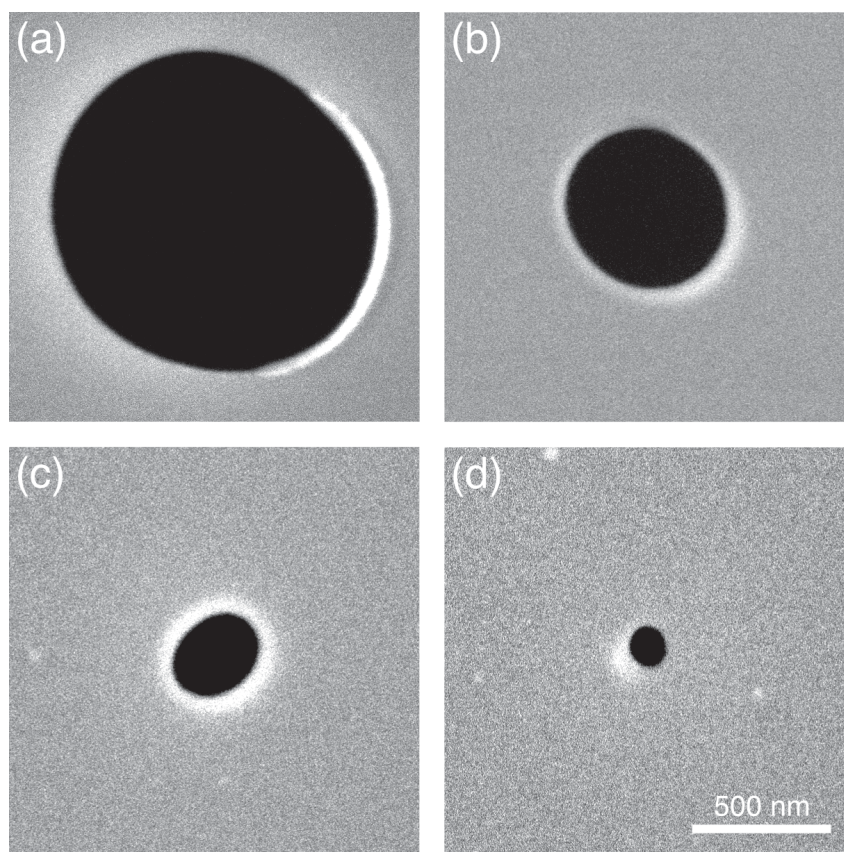

Figure 4.7: SEM images of nanopores in silicon nitride membranes: (a) 1,160 nm diameter, (b) 587 nm, (c) 302 nm, and (d) 119 nm. Scale bar, 500 nm.
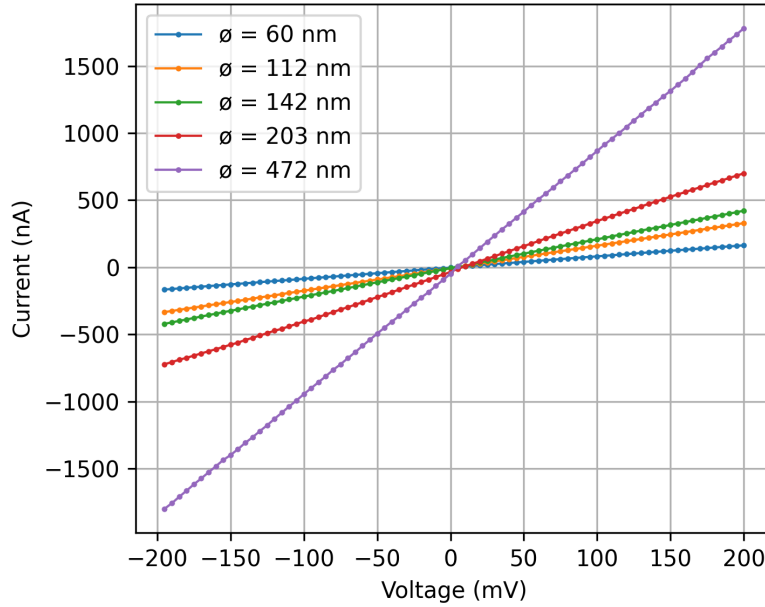
Figure 4.8: Current–voltage curves for nanopores with diameters of 60 nm (blue), 112 nm (orange), 142 nm (green), 203 nm (red) and 472 nm (purple).

results. All pores exhibit ohmic behavior, with current linearly proportional to applied potential.

The measured conductance values agree with the total conductance model G_{total} (Equation 4.3), which includes access conductance. For larger pores, the channel conductance $G_{channel}$ (Equation 4.1) increases rapidly, causing overall conductance to be dominated by access conductance G_{access}.

Measured conductance consistently exceeds the prediction for the actual membrane thickness $t = 45.6$ nm. This discrepancy can arise from pore geometries, which may not be perfectly cylindrical. Focused ion beam milling can produce hourglass or conical profiles that increase conductance compared to ideal cylinders [2].

To account for this effect, an effective membrane thickness t_{eff} is defined as the thickness that minimizes the least-squares error between the analytical model and experimental data. Fitting Equation 4.3 to the measurements yields $t_{eff} = 22.0$ nm.

Oxygen plasma treatment is essential for proper nanopore function. Previous studies suggest that O_2 plasma converts the superficial silicon nitride layer into silicon dioxide [3, 4]. Since SiO_2 is highly hydrophilic, the treatment enhances surface and pore wettability. Contact angles of water on silicon nitride were measured with a goniometer (Ramè-hart Instrument Co.). Figure 4.10 shows the contact angle
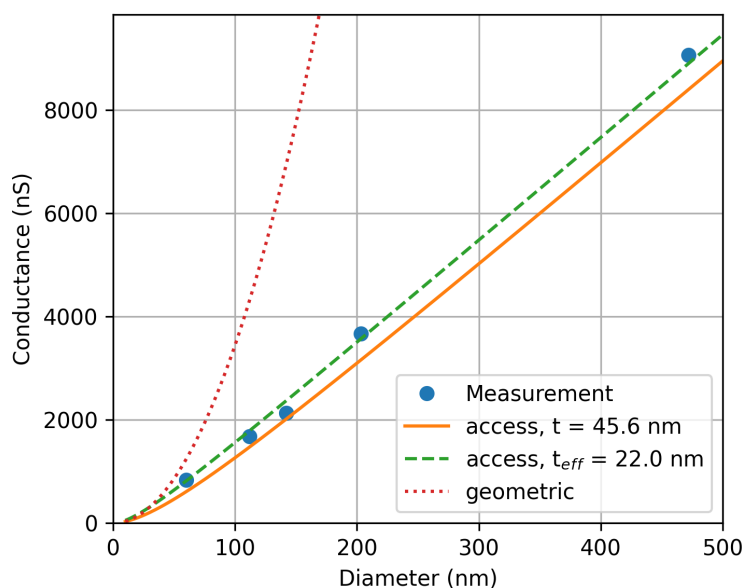
Figure 4.9: Conductance of pores with various diameters: measured values (blue circles); total conductance model (G_{total}, Equation 4.3) with membrane thickness of 45.6 nm (solid orange); total conductance model with fitted thickness of 22.0 nm (dashed green); channel conductance model (G_{channel}, Equation 4.1) (dotted red).
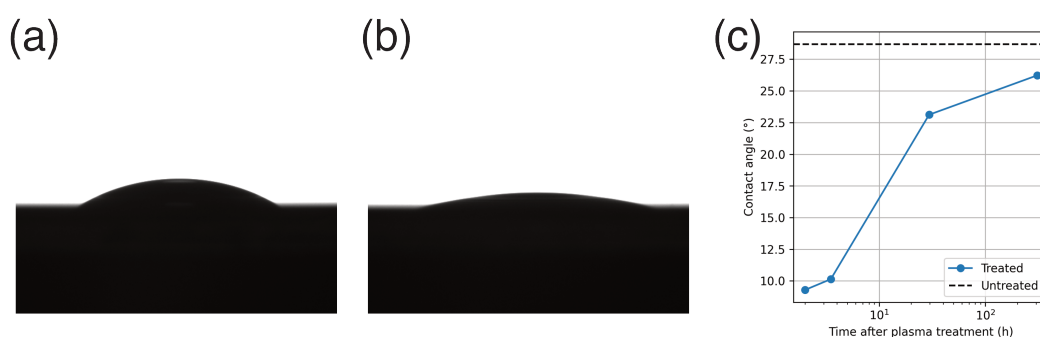

Figure 4.10: Contact angle measurements on SiN_x surfaces. (a) Water droplet on an untreated SiN_x layer. (b) Water droplet on SiN_x 2 hours after O_2 plasma treatment. (c) Contact angle versus time after plasma treatment.
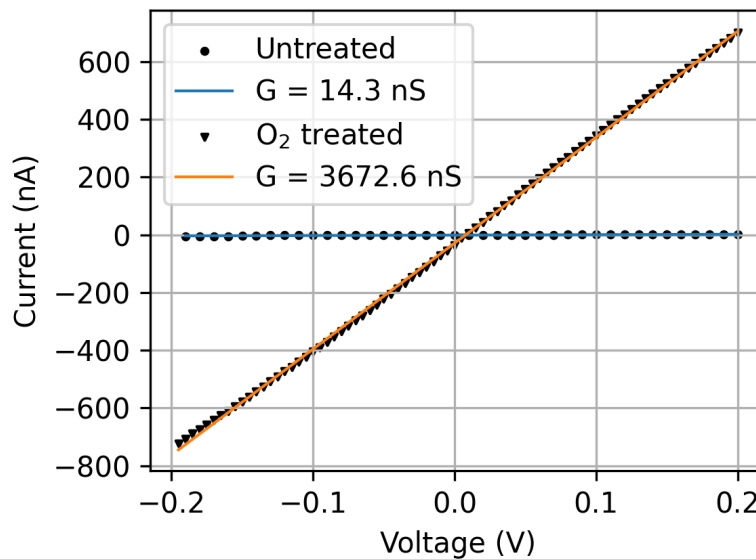
Figure 4.11: Current–voltage curves for a 203 nm diameter pore before (circle markers) and after (triangle markers) O_2 plasma treatment.

decreasing from 28.7° to 9.3° after plasma treatment.

A hydrophobic surface impedes electrolyte filling of the pore, degrading conductance. Figure 4.11 compares I–V curves for the same pore before and after O_2 plasma treatment. Plasma exposure increased conductance by a factor of 257.

4.5   Conclusion

This chapter presented analytical and numerical models of nanopore conductance, validated by experiments. Numerical simulations elucidated how conductance varies with membrane thickness, pore diameter and translocating particles. Experimental measurements agreed with theoretical predictions, with discrepancies attributed to noncylindrical pore geometries. Surface treatment was shown to be necessary for reliable nanopore performance.

Reference

1. Hall, J. E. Access resistance of a small circular pore. *The Journal of General Physiology* **66,** 531–532 (1975).

2. Kowalczyk, S. W., Grosberg, A. Y., Rabin, Y. & Dekker, C. Modeling the conductance and DNA blockade of solid-state nanopores. *Nanotechnology* **22,** 315101 (2011).

3. Jime´nez, C., Perrie´re, J., Vickridge, I., Enard, J. & Albella, J. Transformation of silicon nitride in oxygen plasma. *Surface and Coatings Technology* **45,** 147–154 (1991).

4. Usenko, A. & Senawiratne, J. Silicon nitride surface conversion into oxide to enable hydrophilic bonding. *ECS Transactions* **33,** 475–483 (2010).

TOWARDS MULTIPLEXED DETECTION OF NANOPORES ON A SINGLE CHIP

Nanopore detectors achieve high throughput in DNA sequencing through long read lengths and device miniaturization. Efforts to further increase throughput have focused on integrating more pores into a single device [1, 2]. The most successful strategy to date miniaturizes the entire detection platform, including membrane, electrodes and readout electronics [3, 4]. This strategy enabled commercialization of nanopore sequencing instruments [5]. Current devices incorporate several thousand nanopores, allowing parallel analysis of many molecules. However, device density remains limited by the requirement that each pore has dedicated readout electronics and a reservoir. Consequently, the footprint of each sensing unit on the chip is set by the readout circuitry and reservoir rather than the pore itself.

An alternative approach uses a single pair of electrodes to monitor an array of pores. One implementation measures ionic current fluctuations as particles translocate randomly through the array [6]. This method can assess particle concentration and size across many pores but cannot assign individual events to specific pores. Another approach employs microfluidic circuits to address pores sequentially [7]. This configuration permits detection at individual sites but does not improve overall throughput because only one pore is active at a time.

This chapter proposes a method for multiplexed nanopore detection. Section 5.1 introduces the detection concept. Section 5.2 presents numerical models that evaluate design feasibility and performance. Section 5.3 describes fabrication of test devices. Section 5.4 outlines future directions for implementing the method.

5.1 Multiplexed Detection in Nanopore Detectors

An embedded pair of electrodes enables detection of translocations through multiple pores. Figure 5.1 illustrates two pores, each incorporating two metal layers. With external electrodes driving an ionic current, each pore can be represented by three resistors: for pore one, R_{11} from the upper electrolyte to the upper embedded electrode, R_{12} between the embedded electrodes and R_{13} from the lower embedded electrode to the lower electrolyte; for pore two, R_{21}, R_{22}, and R_{23}, respectively.
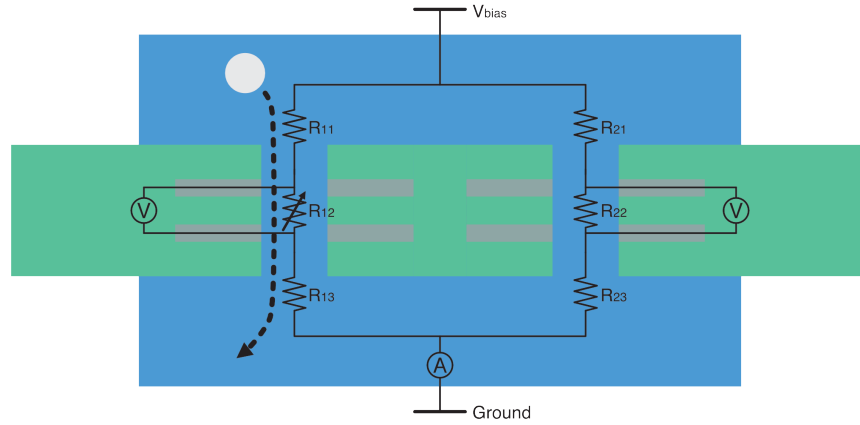
Figure 5.1: Equivalent circuit of a two-pore system. A bias voltage V_{bias} and ground drive ionic current through both pores. An ammeter measures the total current. Embedded electrodes within each pore are connected to voltmeters to monitor the potential difference across each pore segment. When a particle translocates, it increases the segment resistance, producing a detectable voltage change at the corresponding voltmeter.

When a particle (white circle) traverses pore one, its channel diameter decreases and R_{12} increases, while R_{22} remains constant.

In this system, an ammeter connected to the bulk electrodes measures the total ionic current through all pores. A translocation event in a single pore produces a current dip but does not localize the event. Additional measurements of the potential differences across R_{12} and R_{22} allow independent monitoring of each pore. In a system with N pores, $N + 1$ signals are collected: the total current and N potential differences. For a two-pore detector, the recorded signals are the total current and two potential differences, as illustrated in Figure 5.2. Current dips (black) indicate a translocation event; the corresponding potential difference trace (blue or orange) identifies which pore the event occurred in.

5.2 Numerical Models

To evaluate the multiplexed detection concept in Section 5.1, two questions are addressed: (1) can embedded electrodes detect particle translocation and (2) can two pores operate and report events independently. Two numerical models were implemented using COMSOL Multiphysics®.
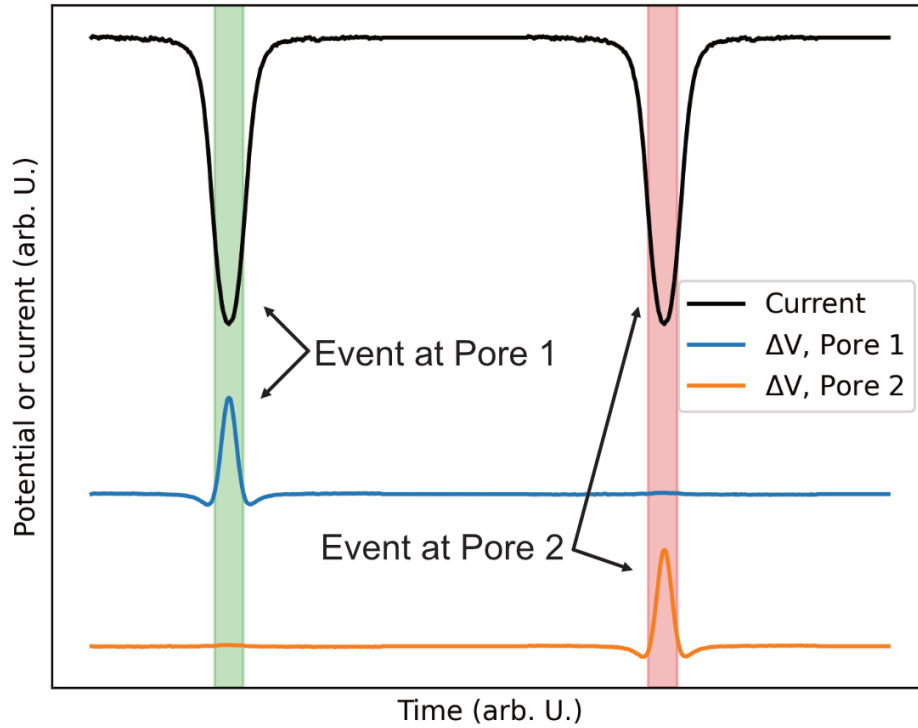
Figure 5.2: Simulated output for a two-pore detector showing total ionic current (black) and potential differences across each pore (blue for pore 1, orange for pore 2). Current dips indicate translocation events; the corresponding potential trace identifies the active pore.

First, a two dimensional axisymmetric model tests the first question. This simplified model includes a single pore and a particle centered on the axis of symmetry. Its computational efficiency permits variation of parameters such as layer thickness and particle size. Figure 5.3 shows a schematic of the device geometry, not to scale. The stack comprises three SiN_x layers of thickness t_{top}, t_{mid} and t_{bot}, separated by platinum electrode layers of thickness t_{elec}. Each layer contains a pore of diameter d_{pore} and the assembly is immersed in electrolyte.

The top and bottom boundaries of the simulation domain serve as bulk electrodes for measuring ionic current. Both are modeled as Ag/AgCl electrodes with a potential
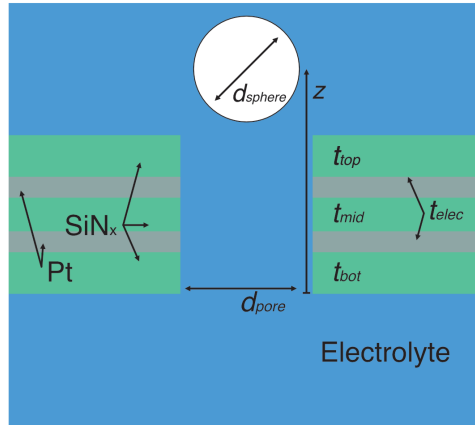
Figure 5.3: Axisymmetric geometry of the 2-D numerical model. Two embedded Pt electrodes of thickness t_{elec} are sandwiched between SiN_x layers of thickness t_{top}, t_{mid} and t_{bot}. A pore of diameter d_{pore} penetrates all layers. The entire domain is filled with electrolyte of conductivity $\sigma = 19.9859$ S/m. An insulating sphere of diameter d_{sphere} is positioned on the axis at a distance z above the membrane bottom.

of +0.197 V relative to the standard hydrogen electrode. During simulation, the membrane top boundary is held at ground and the bottom boundary at –1.0 V. Each embedded electrode is connected to ground through a 100 MΩ resistor to represent the input impedance of a differential amplifier. The electrolyte conductivity is set to $\sigma = 19.9859$ S/m.

Translocation of an insulating sphere of diameter d_{sphere} was simulated under steady-state conditions, computing equilibrium potential and current at each sphere position z. All SiN_x layers were set to 50 nm ($t_{top} = t_{mid} = t_{bot} = 50$ nm) and the embedded electrodes to 25 nm ($t_{elec} = 25$ nm), for a total stack thickness of 200 nm. The pore diameter was $d_{pore} = 200$ nm.

Figure 5.4(a–c) presents the electrolyte potential distribution near the pore with the sphere at $z = 550$ nm, $z = 150$ nm and $z = 50$ nm above the membrane bottom. In Figure 5.4(a), the sphere is distant from the pore and the potential field is unperturbed. As the sphere enters the pore (Figures 5.4(b–c)), the potential distribution becomes distorted, reflecting the reduced cross-sectional area available for ionic current flow.

As discussed in Section 5.1, changes in electrolyte potential within the pore during translocation affect the potentials of the embedded electrodes. The difference
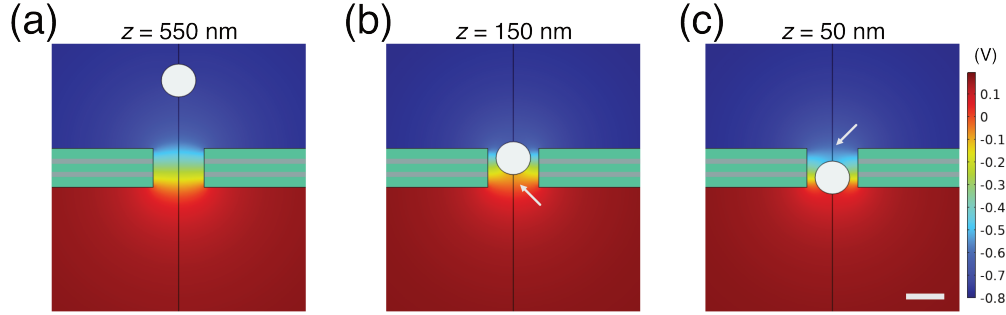
Figure 5.4: Electrolyte potential distribution near a 200 nm pore during a simulated translocation event, with the sphere positioned at (a) $z = 550$ nm, (b) $z = 150$ nm, and (c) $z = 50$ nm above the membrane bottom. The top and bottom external electrodes are held at -1.0 V and 0 V, respectively. Arrows indicate changes in the potential field. Scale bar: 100 nm.

between these electrode potentials can be used to detect translocation events. Simulations were performed for spheres with diameters ranging from 30 nm to 190 nm to evaluate changes in electrode potential and ionic current during translocation.

Figure 5.5(a) shows the potential measured at the upper (solid lines) and lower (dotted lines) embedded electrodes. Line color indicates sphere diameter. As the sphere moves through the channel ($0 < z < 0.2$ μm), transient fluctuations are observed in the embedded electrode potentials. The resulting potential difference is shown in Figure 5.5(b), while the ionic current measured through the bulk electrodes is shown in Figure 5.5(c). The potential difference and current signals are temporally correlated, indicating that translocation events can be identified by monitoring the potential difference between embedded electrodes.

Pulse amplitude increases with particle diameter. The amplitude of each voltage and current signal was calculated as the difference between its maximum and minimum values (Figure 5.6(a)). Figures 5.6(b) and 5.6(c) show that both voltage and current amplitudes scale with particle size due to greater obstruction of the ionic channel. These results indicate that pulse amplitude may be used to estimate particle diameter during translocation.

One key design parameter is the thickness of the middle SiN_x layer, t_{mid}. This layer determines the separation between the embedded electrodes and influences both the shape and amplitude of voltage pulses during translocation. To evaluate this effect, translocations of a 170 nm sphere through a 200 nm pore were simulated while varying t_{mid} from 10 nm to 110 nm.
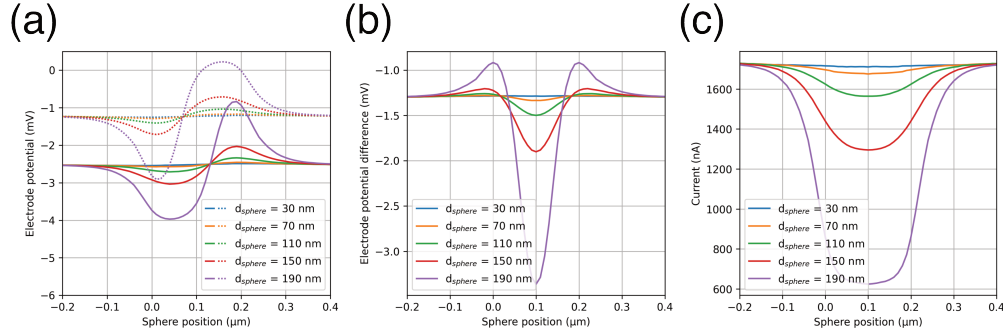
Figure 5.5: Numerical simulation results for translocation of spheres with varying diameters d_{sphere} through a 200 nm pore. (a) Electrode potentials on the upper (solid) and lower (dotted) embedded electrodes. (b) Potential difference between the two embedded electrodes. (c) Ionic current through the pore measured at the bulk electrodes.
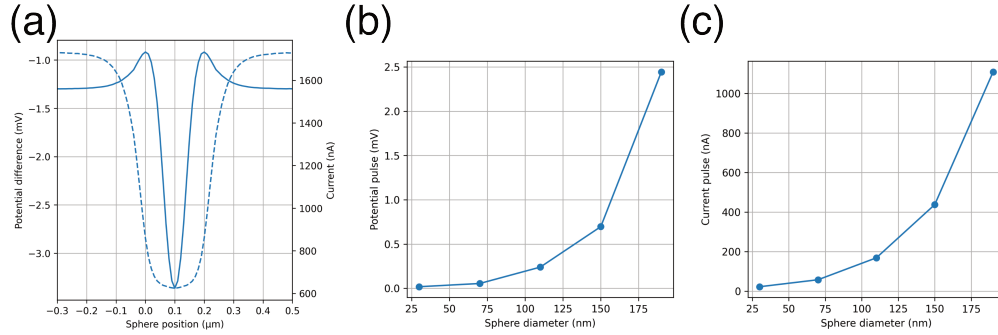

Figure 5.6: Potential and current pulse during translocations. (a) Example signals showing the potential difference between embedded electrodes (solid) and ionic current through the pore (dashed). Pulse amplitude is defined as the difference between maximum and minimum values. (b) Potential pulse amplitude as a function of sphere diameter. (c) Current pulse amplitude as a function of sphere diameter.

Figure 5.7(a) shows the potential difference signals during translocation for various t_{mid} values. As the total membrane thickness increases, the center position of the pulse shifts. Figure 5.7(b) shows that the voltage pulse amplitude increases with larger t_{mid}, due to the extended region over which the potential is modulated. In contrast, the current pulse amplitude decreases with increasing t_{mid} because the longer pore length reduces channel conductance (see Equation 4.1). Consequently, the lower baseline current results in smaller current pulses.

In summary, the 2-D numerical model demonstrated that translocation events can be detected by measuring the potential difference between embedded electrodes. The simulations also showed that pulse amplitude correlates with sphere diameter,
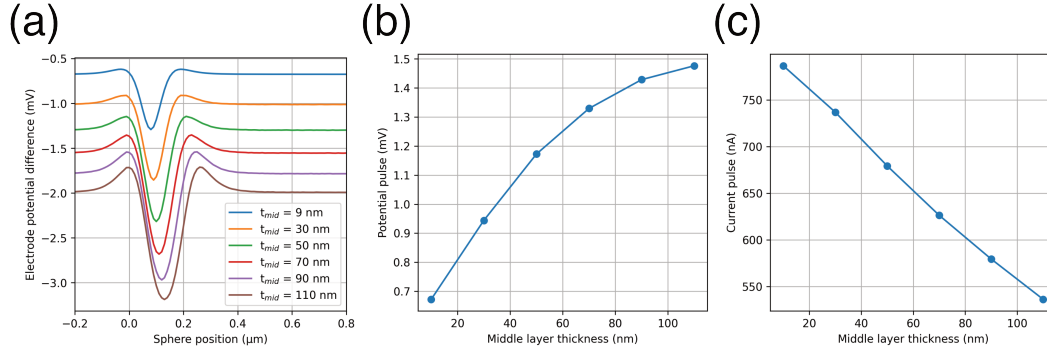
Figure 5.7: Effect of the middle layer thickness on voltage pulse. (a) Potential difference between embedded electrodes during translocation of a 170 nm sphere through a 200 nm pore, for various middle layer thicknesses t_{mid}. (b) Voltage pulse amplitude as a function of t_{mid}. (c) Current pulse amplitude as a function of t_{mid}.

suggesting the possibility of estimating particle size from the electrode signal. Finally, simulations with varying middle layer thickness (t_{mid}) revealed a trade-off between voltage pulse amplitude and pore conductance, indicating that optimal detector performance requires balancing these parameters.

One important question not addressed by the 2-D simulations is whether multiple pores can independently detect translocation events without crosstalk. To investigate this, a 3-D numerical model was developed using COMSOL Multiphysics®. Figure 5.8 shows the xz-plane of the model along with the geometric parameters.

Each pore is constructed with three 50 nm thick SiN$_\text{x}$ layers ($t_{\text{top}} = t_{\text{mid}} = t_{\text{bot}} = 50$ nm) and two embedded platinum electrodes, each 25 nm thick ($t_{\text{elec}} = 25$ nm). The two pores are separated by 2 μm. All 3-D simulations modeled the translocation of a 170 nm diameter sphere through a 250 nm diameter pore (Pore 1), while no particle was placed near Pore 2.

Electrical properties in the 3-D model were identical to those in the 2-D simulations. The top and bottom planes of the simulation domain served as bulk electrodes to drive and measure ionic current. The top electrode was held at ground and the bottom at –1.0 V. Each of the four embedded electrodes was independently connected to ground through a 100 MΩ resistor to simulate potential measurement via high-impedance differential amplifiers. The electrolyte conductivity was set to σ = 19.9859 S/m.

The electrolyte potential distribution was first computed to evaluate the local effect of translocation. Figures 5.9(a–c) show the potential distribution when the 170 nm
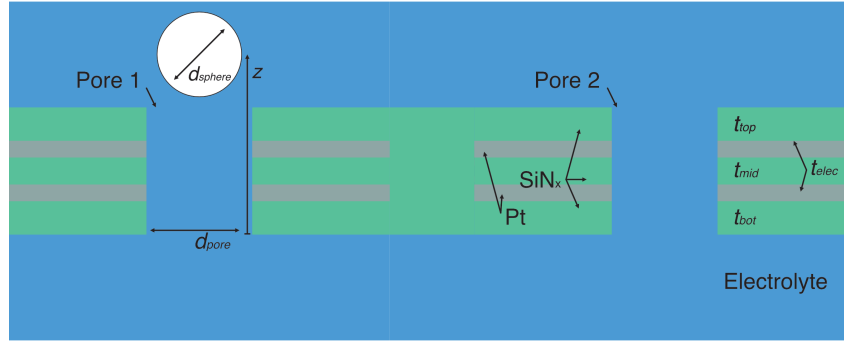
Figure 5.8: Geometry used in the 3-D numerical model. Two pores are formed in a membrane, each with a pair of embedded Pt electrodes. The electrodes are encapsulated by SiN$_x$ layers of thickness t_{top}, t_{mid}, and t_{bot}. Both pores and the surrounding region are immersed in electrolyte. A translocating sphere is introduced only in Pore 1.

sphere is located at $z = 150$ nm, $z = 50$ nm, and $z = -400$ nm relative to the bottom of the membrane. As in the 2-D model, the presence of the sphere alters the potential distribution within Pore 1, while the potential distribution in Pore 2 remains unaffected.

Potential measured at the embedded electrodes is shown in Figure 5.10(a). The signals from Pore 1 (blue) exhibit fluctuations on both electrodes during translocation, while the signals from Pore 2 (orange) remain constant. Figure 5.10(b) shows that the potential difference between the embedded electrodes in Pore 1 is correlated with a dip in the total ionic current. These results indicate that the specific pore in which a translocation occurs can be identified by monitoring the potential difference across its embedded electrodes. This approach may thus enable independent event detection in a multipore detector.

One advantage of the 3-D model is that it allows simulation of off-axis translocations, which are not accessible in the axisymmetric 2-D geometry. In this simulation set, a 170 nm sphere translocates through Pore 1 (250 nm diameter) with lateral offsets of 0 nm, 15 nm, and 30 nm from the pore's center axis. Figure 5.11(a) shows the potential difference measured from Pore 1 (solid lines) and Pore 2 (dotted lines) for each offset: 0 nm (blue), 15 nm (orange), and 30 nm (green). Figure 5.11(b) shows the corresponding ionic current through the bulk electrodes during translocation.
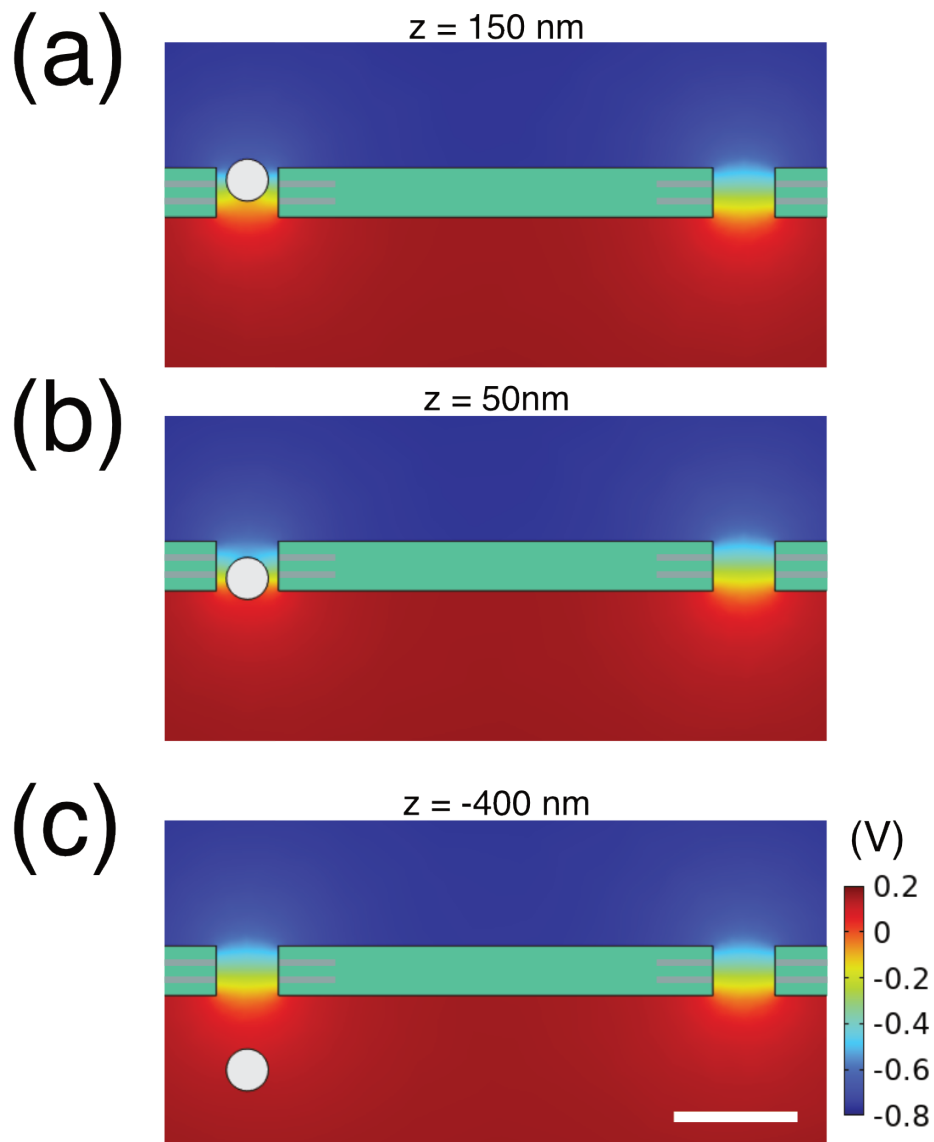
Figure 5.9: Electrolyte potential distribution near two pores in the 3-D numerical simulation. The pore and sphere diameters are 250 nm and 170 nm, respectively, and the pores are separated by 2 μm. The sphere is positioned at (a) $z = 150$ nm, (b) $z = 50$ nm, and (c) $z = -400$ nm relative to the bottom of the membrane. Cross-sections are shown in the xz-plane. Scale bar: 500 nm.
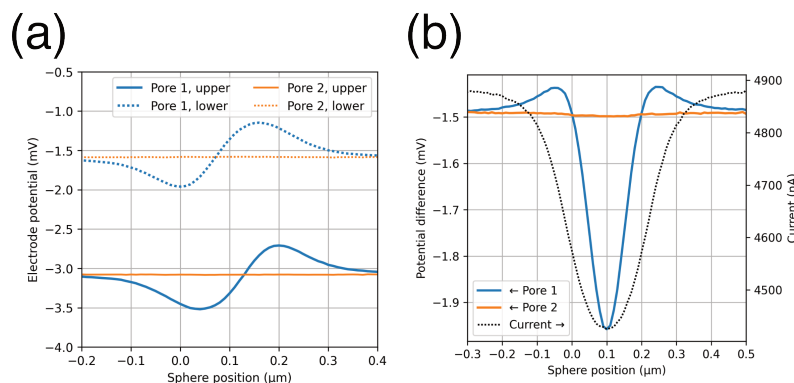
Figure 5.10: Potential and current measurements during translocation of a 170 nm sphere through one of two 250 nm pores. (a) Electrode potentials at each embedded electrode. As the sphere translocates through Pore 1, the embedded electrodes in Pore 1 show potential changes (blue), while those in Pore 2 remain constant (orange). (b) Potential difference between embedded electrodes (solid) and total transmembrane current (dotted).
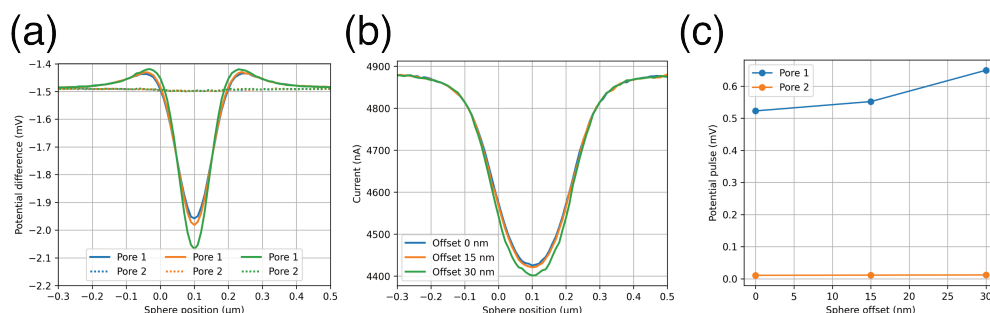

Figure 5.11: (a) Potential difference between embedded electrodes in Pore 1 (solid) and Pore 2 (dotted) during translocation of a 170 nm sphere through a 250 nm pore with lateral offsets of 0 nm (blue), 15 nm (orange), and 30 nm (green) from the center. (b) Ionic current measured during the translocation for each offset. (c) Amplitude of potential pulses as a function of lateral offset.

The results indicate that lateral offset does not significantly affect the amplitude or shape of voltage and current pulses. Therefore, detector performance is robust to off-axis translocation events.

In summary, the 3-D simulations confirm that only the pore through which a particle translocates exhibits fluctuations in the embedded electrode signals, while neighboring pores remain unaffected. These potential fluctuations are correlated with dips in the total ionic current, enabling identification of the active pore. Additionally, lateral offsets of up to 30 nm from the pore axis do not significantly affect the shape

or amplitude of the voltage or current pulses, indicating robust detector performance for off-center translocations. These results demonstrate that embedding electrodes around each pore enables independent readout channels for multiplexed nanopore sensing.

5.3 Device Fabrication

To demonstrate the multiplexed measurement scheme proposed in Section 5.1, nanopore sensors with embedded electrodes were fabricated. The process begins with a double-side polished silicon wafer coated with 50 nm of LPCVD SiN_x (Rogue Valley Microdevices), as illustrated in Figure 5.12(a). Marker patterns in Au were first defined to assist with subsequent alignment steps.

A 200 nm layer of 950K poly(methyl methacrylate) (PMMA, MicroChem Corp.) was spin-coated and patterned by an electron beam lithography system (EBPG5200, Raith) operating at 100 kV (Figure 5.12(b)). A 25 nm Pt layer with a 2 nm Ti adhesion layer was deposited (Figure 5.12(c)) and followed by a lift-off process to define the bottom electrodes (Figure 5.12(d)). A 50 nm SiN_x insulation layer was then deposited by atomic layer deposition (ALD, FlexAL II, Oxford Instruments) to encapsulate the bottom electrodes (Figure 5.12(e)).

The electron beam lithography, Pt deposition, and ALD steps were repeated to form the top electrode and its insulation layer (Figure 5.12(f)). Next, 1.2 μm of Microposit S1813 photoresist was spin-coated and patterned via photolithography to expose the contact pad regions. The top encapsulating SiN_x layer was plasma-etched (see Appendix A) using the photoresist as a mask to expose the underlying Pt contact areas (Figure 5.12(h)). A 100 nm Au layer with a 10 nm Ti adhesion layer was deposited via electron beam evaporation (Figure 5.12(i)) and lifted off to form electrical contact pads (Figure 5.12(j)). At this stage, the embedded electrode structure was complete.

To fabricate the suspended membrane, the wafer back side was processed. The front side was protected with a 200 nm PMMA layer. The back side was coated with 1.3 μm AZ 5214-E photoresist (Merck Performance Materials GmbH) and patterned using the mask aligner (MA6/BA6, SUSS MicroTec) in back-side alignment mode. The exposed LPCVD nitride was etched by plasma to define the etch window (Figure 5.12(k)). Finally, the silicon substrate was removed in hot KOH solution (see Appendix B), forming suspended SiN_x membranes (Figure 5.12(l)).

The wafer was then diced into individual chips. Nanopores were fabricated on each

chip using Ga$^+$ focused ion beam (FIB) milling. Each chip was imaged in a scanning electron microscope (Nova 600, Thermo Fisher) to locate the embedded electrodes, and nanopores of various sizes were milled directly into the Pt electrode regions (Figure 5.12(m)).

The fabricated multipore sensors were first examined under optical and electron microscopes. Figures 5.13(a) and 5.13(b) show the top and back sides of the membrane, respectively, imaged with an optical microscope. The two electrodes appear in different colors due to variations in thickness of the encapsulating ALD SiN$_x$ layers. The same structure imaged under a scanning electron microscope (SEM) is shown in Figure 5.13(c). A close-up of a membrane region with a pair of electrodes is shown in Figure 5.13(d); the top and bottom electrodes overlap within the hexagonal area, forming the region used for nanopore fabrication.

Pores were drilled using a gallium FIB on two of the embedded electrodes. Figure 5.14(a) shows an overview image of the two pores formed on separate electrodes. Higher magnification images of each pore are presented in Figures 5.14(b) and 5.14(c), respectively. Both pores were fabricated with a diameter of 275 nm.

5.4 Future Work

Experimental work is ongoing in the Nanofabrication group. The feasibility of the detection method and fabrication process for multipore detectors has been demonstrated. The next step is to develop mechanical fixtures to provide fluidic and electrical connections between the chip and the measurement system, as well as to implement transimpedance amplifiers and differential amplifiers for reading ionic currents and voltage signals. Future efforts will focus on demonstrating device operation by detecting translocation events in multiple pores simultaneously.
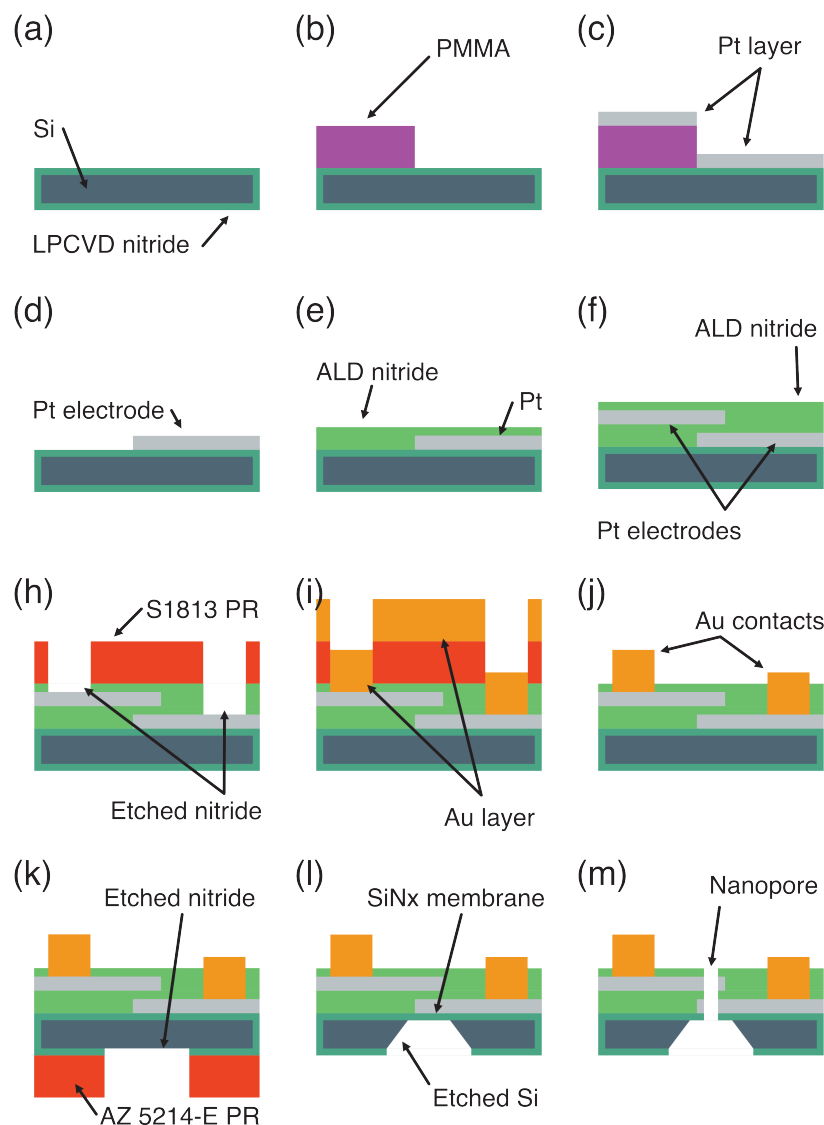
Figure 5.12: Fabrication process of multipore sensors. (a) A silicon wafer coated with LPCVD nitride is prepared. (b) A resist layer is patterned by electron beam lithography. (c) A Pt layer is deposited, and (d) lift-off forms the Pt electrode pattern. (e) A conformal SiN$_x$ layer is deposited via ALD, and (f) steps (b – e) are repeated for a second Pt electrode. (h) Photolithography defines the contact pads, and plasma etching removes the SiN$_x$ covering the electrodes. (i) A Au layer is deposited, and (j) lift-off removes the photoresist and Au, forming the electrode contacts. (k) The wafer's back side is photoresist-coated and patterned to open a window. Plasma etching removes the nitride to expose Si. (l) The Si is wet etched to create a SiN$_x$ membrane on the top side. (m) A nanopore is then patterned by FIB.
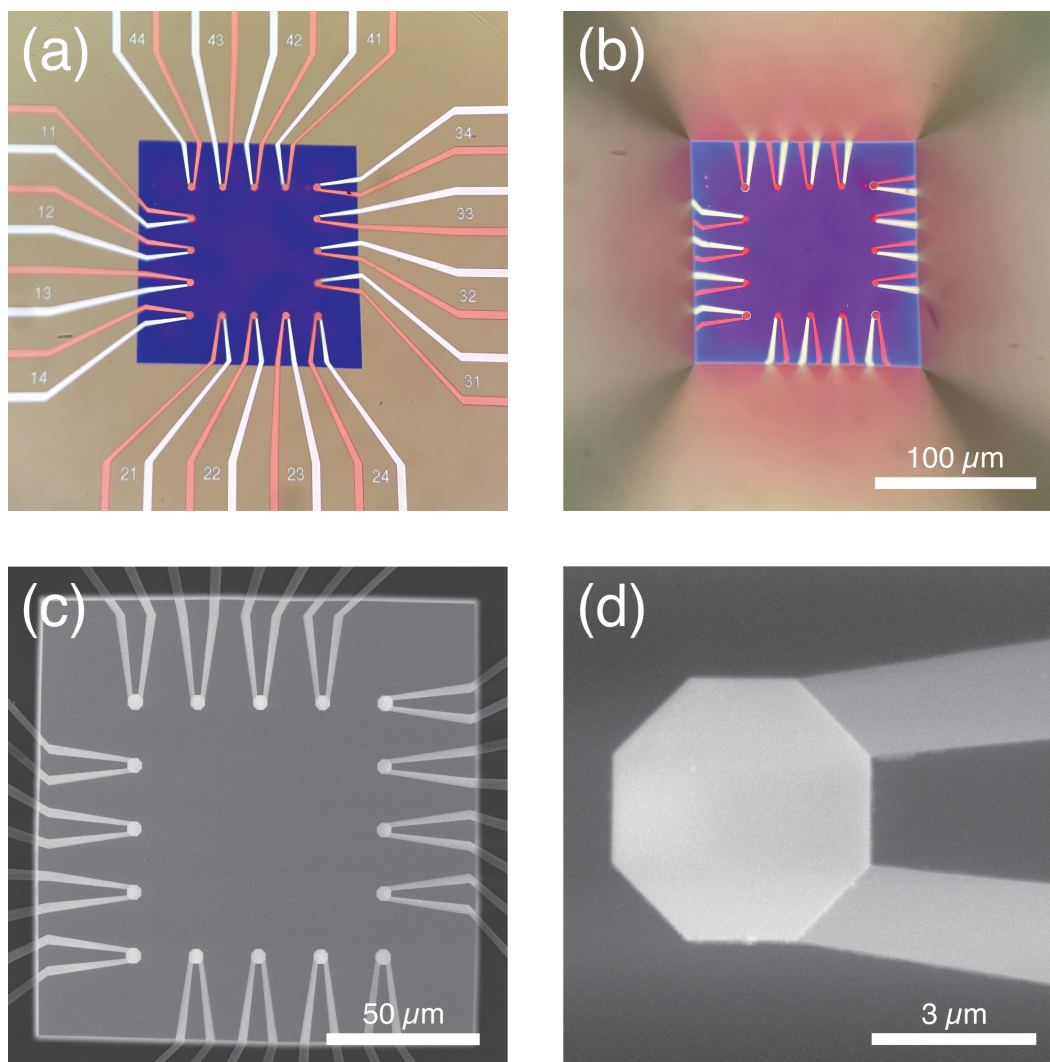
Figure 5.13: Optical microscope images of the membrane area of a multipore sensor: (a) top side and (b) back side of the wafer. Scale bar: 100 μm. Scanning electron microscope images: (c) electrodes on the nitride membrane. Scale bar: 50 μm; (d) close-up of a pair of overlapping electrodes. Scale bar: 3 μm.
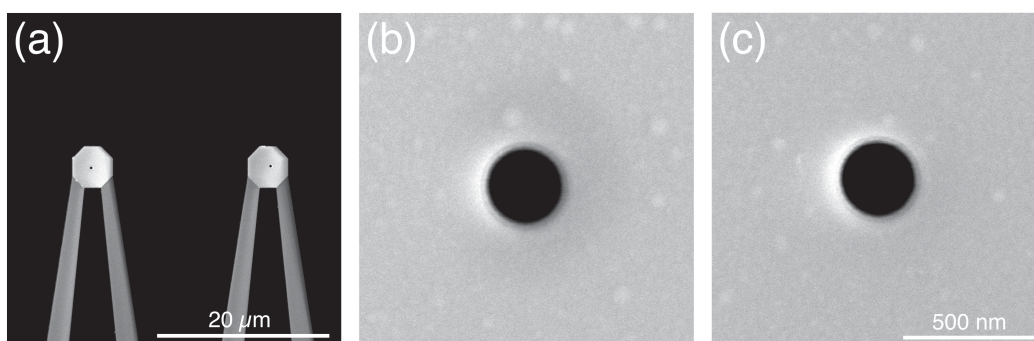
Figure 5.14: SEM images of nanopores fabricated on a multiplexed detector. (a) Overview showing pores on two pairs of embedded electrodes. Scale bar: 20 µm. (b) Close-up of a 275 nm pore on the left electrode pair. (c) Close-up of a 275 nm pore on the right electrode pair. Scale bar: 500 nm.

Reference

1. Rosenstein, J. K., Wanunu, M., Merchant, C. A., Drndic, M. & Shepard, K. L. Integrated nanopore sensing platform with sub-microsecond temporal resolution. *Nature Methods* **9,** 487–492 (2012).

2. Uddin, A. *et al.* Integration of solid-state nanopores in a 0.5 μm CMOS foundry process. *Nanotechnology* **24,** 155501 (2013).

3. Magierowski, S., Huang, Y., Wang, C. & Ghafar-Zadeh, E. Nanopore-CMOS Interfaces for DNA Sequencing. *Biosensors* **6,** 42 (2016).

4. Dawji, Y., Habibi, M., Ghafar-Zadeh, E. & Magierowski, S. A scalable discrete-time integrated CMOS readout array for nanopore based DNA sequencing. *IEEE Access* **9,** 155543–155554 (2021).

5. Jain, M., Olsen, H. E., Paten, B. & Akeson, M. The Oxford Nanopore MinION: delivery of nanopore sequencing to the genomics community. *Genome Biology* **17,** 239 (2016).

6. Wen, C., Zeng, S., Zhang, Z. & Zhang, S.-L. Group Behavior of Nanoparticles Translocating Multiple Nanopores. *Analytical Chemistry* **90,** 13483–13490 (2018).

7. Zeng, S., Wen, C., Zhang, S.-L. & Zhang, Z. A Nanopore Array of Individual Addressability Enabled by Integrating Microfluidics and a Multiplexer. *IEEE Sensors Journal* **20,** 1558–1563 (2020).

Chapter 6

CONCLUSION

This thesis presented three distinct approaches to chemical and molecular detection, each designed to improve footprint, sensitivity, and scalability. A compact mid-infrared (mid-IR) spectrometer, a tunable diode laser absorption spectroscopy (TDLAS) platform for methane detection, and multiplexed solid-state nanopore sensors offer improvements in various applications.

In Chapter 2, a compact mid-IR spectrometer was developed using a continuously variable optical filter based on Ge/BaF_2 structures and a 2D microbolometer array. This system addresses the need for portable and cost-effective infrared spectroscopy in the long-wave infrared (LWIR) fingerprint region (7.5–10.5 μm), where many organic molecules have distinct absorption features. The continuously variable filter produces spatially resolved wavelength dispersion without moving parts, and the 2D microbolometer array enables the integration of spectral data across 13,000 pixels, improving the signal-to-noise ratio through averaging and deconvolution. Spectral measurements of solids, gases, and liquids were demonstrated and validated against commercial FTIR data. This system lays the groundwork for field-deployable mid-IR spectroscopy for material identification and environmental sensing.

Chapter 3 described the development of a TDLAS system optimized for methane detection. TDLAS provides high sensitivity by modulating the laser wavelength near an absorption line and detecting the resulting harmonic signals via lock-in amplification. Both free-space and fiber-coupled configurations were implemented, and a theoretical model was developed to understand signal formation and demodulation. Experiments demonstrated a detection limit of 0.501 ppm-m for the free-space system, with the ability to monitor multiple remote locations using retroreflectors and galvanometer-controlled beam steering. Real-time gas sensing was demonstrated for both free-space and fiber-based systems. This work highlights the potential of cost-effective implementation of TDLAS for industrial gas leak detection, environmental monitoring, and integration with distributed sensor networks.

In Chapter 4, the conductance of solid-state nanopores was investigated both experimentally and through numerical modeling. Analytical and simulation-based models were used to understand how pore geometry and access resistance contribute to the

total conductance. Experimental data obtained from nanopores fabricated in silicon nitride membranes showed agreement with theoretical predictions. Oxygen plasma treatment was found to be essential for improving pore wettability and conductance stability.

In Chapter 5, a new design for multiplexed nanopore sensing was proposed, incorporating embedded electrodes within each pore. Simulations in both 2-D and 3-D demonstrated that translocation events can be independently detected at each pore by monitoring potential differences across the embedded electrodes, even for off-center translocation events. Future works to be done to experimentally prove the multiplexed nanopore design.

CHARACTERIZATION OF PLASMA ETCHING OF SIN$_\text{x}$

Etching of silicon nitride (SiN$_\text{x}$) is a critical step in the fabrication of nanopore devices developed in this thesis. Two types of SiN$_\text{x}$ are used in the fabrication process of the multiplexed nanopore device. First, a low-pressure chemical vapor deposition (LPCVD) nitride film covers both sides of the wafer and serves as a hard mask during the bulk silicon etch. Second, atomic layer deposition (ALD) SiN$_\text{x}$ is used to insulate the embedded electrodes and is later etched to expose electrical contact pads. While both layers are nominally SiN$_\text{x}$, they exhibit different properties. LPCVD SiN$_\text{x}$ typically has a higher density [1] and greater etch resistance compared to ALD SiN$_\text{x}$. This is reflected in ellipsometry measurements: the refractive index of LPCVD SiN$_\text{x}$ is $n = 2.20$, whereas that of ALD SiN$_\text{x}$ is $n = 1.89$.

Photoresists S1318 and AZ5214E are used as etch masks for the respective nitride etching steps. While selectivity is considered, it is not a major constraint in this process, as the SiN$_\text{x}$ layers to be etched are less than 100 nm thick, while the photoresist layers exceed 1 μm in thickness. As a result, the required selectivity is only about 0.1.

Nevertheless, a slower etch rate is preferred to improve process control and repeatability. A target etch rate of approximately 20 nm/min was set for the LPCVD SiN$_\text{x}$, allowing 50 nm of material to be removed in 150 s.

Plasma etching was carried out using an inductively coupled plasma reactive ion etcher (ICP-RIE; Plasmalab System 100, Oxford Instruments) with SF$_6$ and O$_2$ plasma [2]. under the following conditions:

- Pressure: 70 mTorr
- Temperature: 15 °C
- RF power: 75 W
- ICP power: 500 W
- SF$_6$ flow: 48 sccm
- O$_2$ flow: 12 sccm.

Etch times of up to 600 s were tested. The remaining film thickness after each etch was measured using a spectroscopic ellipsometer (M-2000, J.A. Woollam), and the
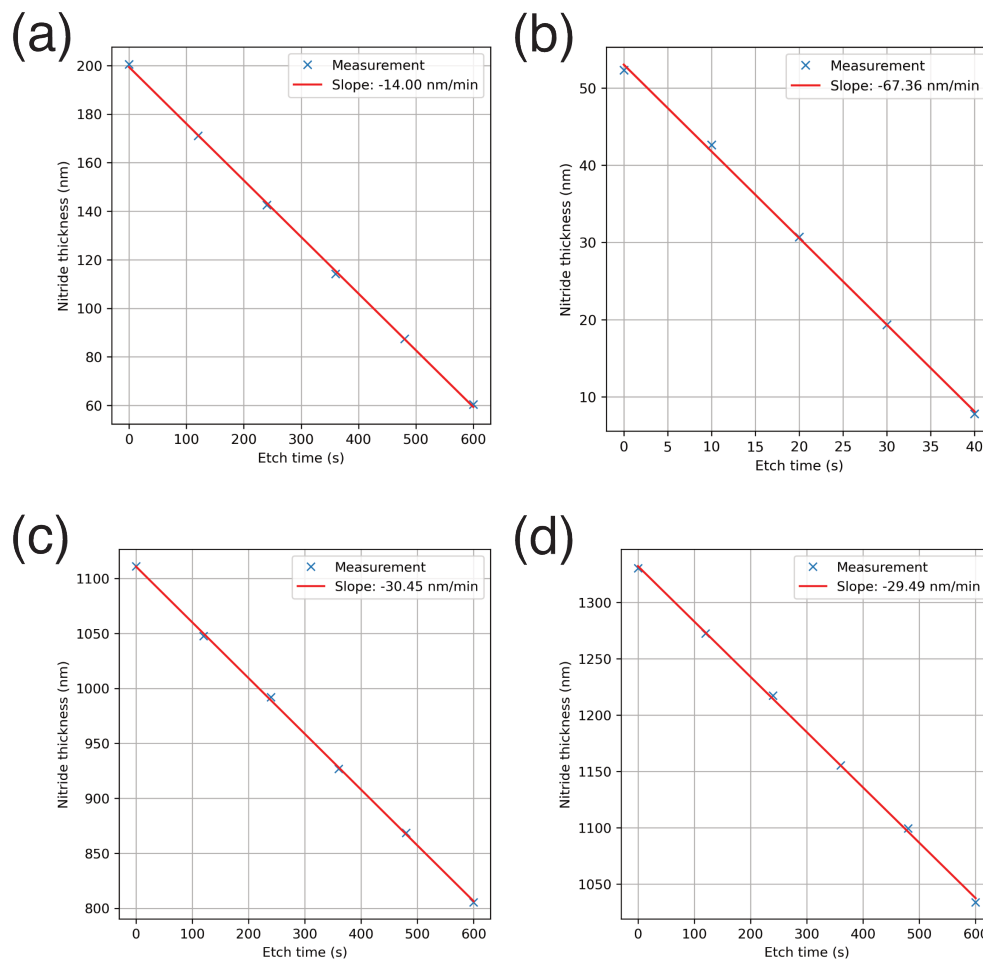
Figure A.1: Remaining film thickness was measured using an ellipsometer after plasma etching. A linear fit was used to determine the etch rate for each material. (a) LPCVD silicon nitride: 14.00 nm/min. (b) ALD silicon nitride: 67.36 nm/min. (c) S1318 photoresist: 30.45 nm/min. (d) AZ5214E photoresist: 29.49 nm/min.

etch rate was extracted by linear fitting. Results are shown in Figure A.1(a–d). The etch rate of LPCVD SiN$_x$ was found to be 14.00 nm/min, while the ALD SiN$_x$ etched much faster at 67.36 nm/min. This 4.8 times difference is attributed to the lower density of the ALD film. The etch rates for the photoresists were 30.45 nm/min for S1318 and 29.49 nm/min for AZ5214E. Accordingly, the selectivity of S1318 was 0.46 against LPCVD SiN$_x$ and 2.21 against ALD SiN$_x$. For AZ5214E, the selectivity was 0.47 and 2.28, respectively.

CHARACTERIZATION OF DEEP ANISOTROPIC SILICON ETCH FOR SIN$_x$MEMBRANE FABRICATION

Throughout this thesis, nanopores are fabricated on silicon nitride membranes. This chapter details the process used to fabricate those membranes and the characterization of the anisotropic silicon etch used. A common technique for forming suspended membranes is anisotropic wet etching of silicon using hot potassium hydroxide (KOH) solution. This process exhibits a characteristic 54.74° sidewall angle, resulting from the significantly slower etch rate in the $\langle 111 \rangle$ direction compared to the $\langle 100 \rangle$ direction [3]. Silicon nitride (SiN$_x$) is used as a hard mask due to its extremely high selectivity against silicon in hot KOH [4].

Two key parameters govern the etching process: the concentration of the KOH solution and the process temperature. Prior studies [3, 5, 6] show that a smooth etched surface is typically obtained at concentrations above 30% (v/v), with the etch rate increasing with temperature. In this work, the KOH concentration and temperature were fixed at 30% (v/v) and 75 °C, respectively. The silicon etch rate was characterized to determine the required etch duration for membrane fabrication.

The etch rate was measured using 3-inch $\langle 100 \rangle$ Si wafers coated with 50 nm of low-stress LPCVD SiN$_x$ (Rogue Valley Microdevices). Square openings (640 μm × 640 μm) were patterned using AZ5214E photoresist and transferred to the SiN$_x$ layer using plasma etching (see Appendix A). These nitride openings served as hard masks for the subsequent wet etch.

Samples were etched in 30% (v/v) KOH at 75 °C for durations ranging from 60 to 180 minutes. The depth of the etch along the $\langle 100 \rangle$ direction was determined from scanning electron microscope (SEM) images (Nova 600, Thermo Fisher Scientific). Due to the anisotropic nature of the etch, sidewalls form at 54.74° to the bottom surface, as shown in Figure B.1(a). The etch depth d was calculated from the top mask width L and the bottom opening width w using:

$$d = \frac{L - w}{2} \tan\left(54.74°\right) \qquad (B.1)$$

Figures B.1(b–f) show SEM images of samples etched for various durations. As expected, the bottom width w narrows with longer etch times. From these measure-
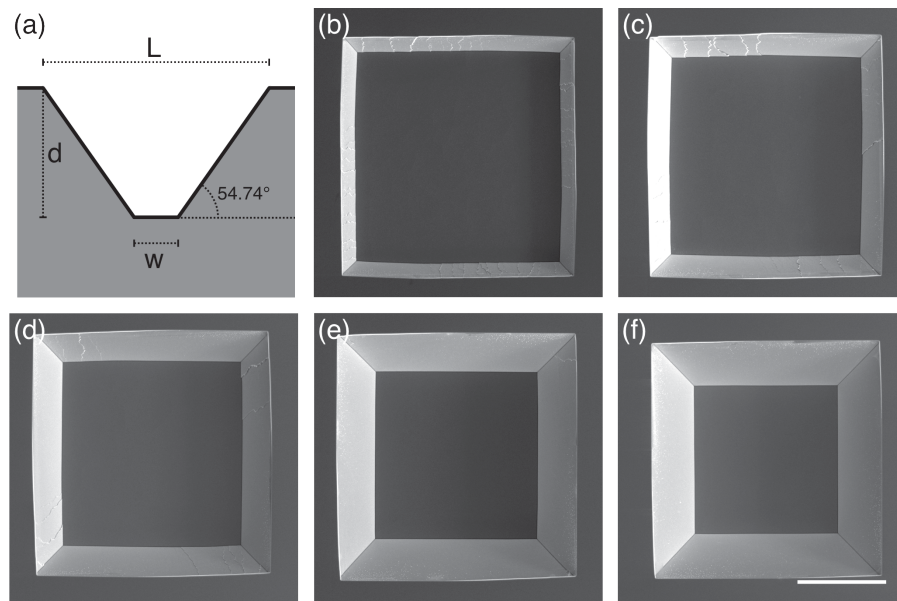
Figure B.1: Scanning electron microscope images of wet etched Si samples. (a) Geometry used to calculate etch depth d from the mask width L and the bottom width w. (b–f) SEM images of etched samples after 60, 90, 120, 150, and 180 minutes. Scale bar: 250 µm.

ments, the etch depth was plotted against etch time (Figure B.2), yielding a linear fit with an etch rate of 1.02 µm/min. Given a wafer thickness of approximately 380 µm, a minimum etch duration of 373 minutes is required. To ensure full membrane release and accommodate process variation, a 20% overetch was applied, resulting in a total etch duration of 450 minutes. An example of a completed silicon nitride membrane is shown in Figure B.3.

The following steps outline the KOH wet etching process used to fabricate silicon nitride membranes:

1. Prepare a 30% (v/v) KOH solution using deionized water.
2. As shown in Figure B.4, place the KOH solution in a beaker on a hotplate. Add a magnetic stir bar and a thermocouple for temperature monitoring.
3. Set the hotplate to 75 °C and stir at 300 rpm. Wait for the temperature to stabilize (typically 1–2 hours).
4. Mount the sample securely in a Teflon holder and immerse it in the KOH solution.
5. After approximately 7 hours (450 minutes), remove the sample and rinse thoroughly with deionized water.
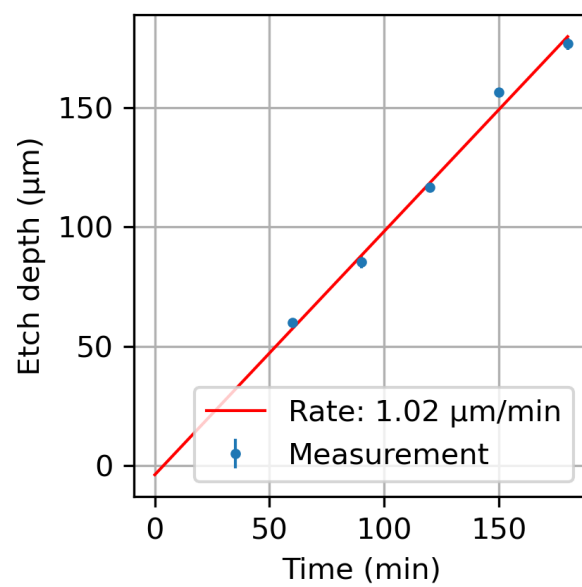6. Dry the sample using a nitrogen (N_2) stream.

Figure B.2: Etch depth versus etch time (blue dots) and linear fit (red line). The measured etch rate in 30% (v/v) KOH at 75 °C is 1.02 µm/min.
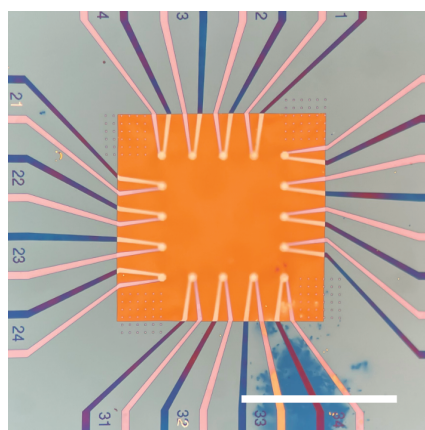

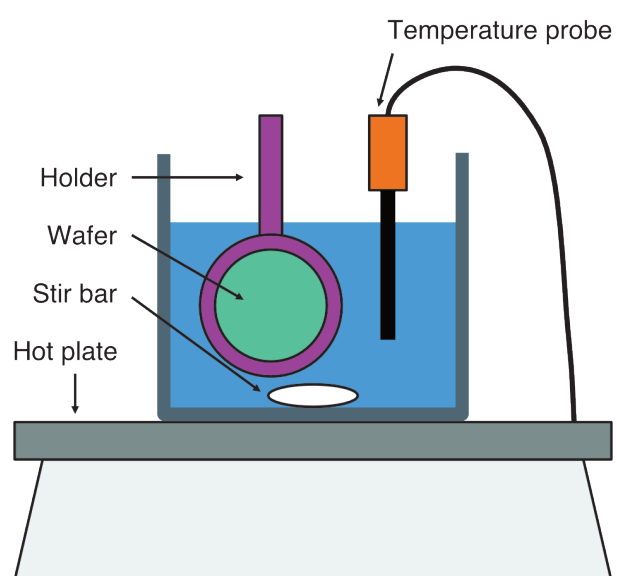Figure B.3: Optical image of a silicon nitride membrane after complete etching. Scale bar: 100 µm.

Figure B.4: Setup for anisotropic Si wet etching using a heated KOH bath with magnetic stirring and temperature control.

Reference

1. Morin, P., Raymond, G., Benoit, D., Maury, P. & Beneyton, R. A comparison of the mechanical stability of silicon nitride films deposited with various techniques. *Applied Surface Science* **260,** 69–72 (2012).

2. De Almeida, F. R., Yamamoto, R. & Maciel, H. S. Reactive ion etching of PECVD silicon nitride in SF6 plasma. *Journal of Nuclear Materials* **200,** 371–374 (1993).

3. Tabata, O., Asahi, R., Funabashi, H., Shimaoka, K. & Sugiyama, S. Anisotropic etching of silicon in TMAH solutions. *Sensors and Actuators A: Physical* **34,** 51–57 (1992).

4. Williams, K., Gupta, K. & Wasilik, M. Etch rates for micromachining processing-Part II. *Journal of Microelectromechanical Systems* **12,** 761–778 (2003).

5. Sato, K. *et al.* Characterization of orientation-dependent etching properties of single-crystal silicon: effects of KOH concentration. *Sensors and Actuators A: Physical* **64,** 87–93 (1998).

6. Tanaka, H., Yamashita, S., Abe, Y., Shikida, M. & Sato, K. Fast etching of silicon with a smooth surface in high temperature ranges near the boiling point of KOH solution. *Sensors and Actuators A: Physical* **114,** 516–520 (2004).